

2023

Spectroscopy And Dynamics Of Atmospherically And Combustion-Relevant Collision Complexes

John Patrick Davis

College of William and Mary - Arts & Sciences, jpdavis01@wm.edu

Follow this and additional works at: <https://scholarworks.wm.edu/etd>



Part of the [Physical Chemistry Commons](#)

Recommended Citation

Davis, John Patrick, "Spectroscopy And Dynamics Of Atmospherically And Combustion-Relevant Collision Complexes" (2023). *Dissertations, Theses, and Masters Projects*. William & Mary. Paper 1686662587. <https://dx.doi.org/10.21220/s2-q91s-1347>

This Thesis is brought to you for free and open access by the Theses, Dissertations, & Master Projects at W&M ScholarWorks. It has been accepted for inclusion in Dissertations, Theses, and Masters Projects by an authorized administrator of W&M ScholarWorks. For more information, please contact scholarworks@wm.edu.

Spectroscopy and Dynamics of Atmospherically and Combustion Relevant Collision
Complexes

John Patrick Davis

Columbia, South Carolina

Bachelor of Science, Washington and Lee University, 2021

A Thesis presented to the Graduate Faculty of The College of William & Mary in
Candidacy for the Degree of
Master of Science

Chemistry Department

College of William & Mary
May 2023

APPROVAL PAGE

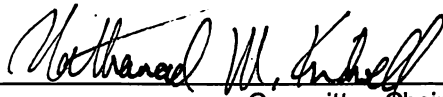
This Thesis is submitted in partial fulfillment of
the requirements for the degree of

Master of Science



John Patrick Davis

Approved by the Committee, April 2023



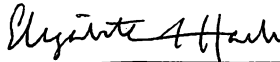
Committee Chair

Nathanael Kidwell, Associate Professor, Chemistry
College of William & Mary



Co-Chair

John C. Poutsma, Professor, Chemistry
College of William & Mary



Co-Chair

Elizabeth J. Harbron, Floyd D. Gottwald, Sr. Professor; Director, Charles Center, Chemistry
College of William & Mary

ABSTRACT

Potential energy surfaces describing bimolecular collisions sensitively depend on the chemical functionality and the relative orientation of colliding partners, thus defining the accessibly reactive and nonreactive pathways. Herein, we investigate the peculiar product outcomes arising from Jahn-Teller distortion of the nitric oxide and methane complex (NO-CH₄).

We have reported an in-depth spectroscopic and dynamics study of NO-CH₄ by utilizing conformation-specific and action spectroscopy, as well as velocity map imaging, to understand the fundamental dissociative mechanisms at play. Ultimately, we have gained information about how the Jahn Teller effect possibly impacts the potential product energy transfer pathways. The distinctly varied product outcomes provide important experimental signatures of a Jahn Teller distorted equilibrium geometry and the ranging effects it can have. Finally, we discuss how subsequent studies will be carried out.

TABLE OF CONTENTS

Acknowledgements	iii
Dedications	iv.
Chapter 1. Introduction	1
1.1. Atmospheric and Combustion Relevance	1
1.2. Laser Spectroscopy	5
1.3. Scope of Thesis	5
1.4. References	7
Chapter 2. Experimental Methods	10
2.1. Experimental Apparatus Description	10
2.2. Supersonic Jet Expansion	11
2.3. Laser Equipment and Methods	13
2.3.1 Ion Optics and Detection Process	14
2.4. Spectroscopic Techniques	16
2.4.1. Resonant-Two-Photon-Ionization	16
2.4.2. Resonant Ion-Depletion Infrared Spectroscopy	17
2.4.3. Infrared Action Spectroscopy	19
2.4.4. Velocity-Map-Imaging	21
2.5. References	24
Chapter 3. Vibrational Spectroscopy of NO-CH ₄	25
3.1. Introduction	25
3.2. Methods	27
3.3. Theoretical Calculations	29
3.4. Results	31

3.5. Discussion	36
3.6. Conclusions	40
3.7. References	41
Chapter 4. Infrared Activated Dynamics of NO-CH ₄	45
4.1. Introduction	45
4.2. Methods	50
4.3. Results	53
4.3.1. Product State Distributions	55
4.4. Discussions	58
4.4.1. Vibrational Predissociation Dynamics	58
4.4.2. Assignment of CH ₄ Vibrational Modes	62
4.4.3. Jahn-Teller Mechanistic Pathways	64
4.5. Conclusions	75
4.6. References	77
Chapter 5. Larger NO-alkane Van der Waals Complexes	79
5.1. Introduction	79
5.2. Previous Studies	80
5.3. Proposed Studies	82
5.3.1. NO-Ethane	83
5.3.2. Higher Order NO-Alkanes	86
5.3.3. Additional Techniques	87
5.4. References	89

ACKNOWLEDGEMENTS

I would like to express my deep gratitude to Dr. Nathanael Kidwell who has been an incredible advisor and mentor. Thank you for your constant support as well as your infectious scientific curiosity. My time in the William & Mary Master's program has been an enlightening experience and an incredible place to do science due to your help, support, and time. I would also like to thank Dr. John C. Poutsma and Dr. Elizabeth J. Harbron for providing their patience, knowledge, expertise, and time in the reading and editing of this manuscript.

I would also like to thank Anna Miller for listening to me talk about anisotropy for a running time of 144 hours. I can never thank you enough for your unwavering support. Finally, I would like to thank and acknowledge all the undergraduates that I have worked with in the Kidwell Lab. I truly have cherished the time that we have spent sciencing.

This thesis is dedicated to everyone who has had a helping hand along the way.

Chapter 1: Introduction

The study of interactions between molecules and atoms is an important research area in physical chemistry, atmospheric chemistry, and energy science. Particularly, at the forefront of these fields, is using light radiation to control and steer the chemical reactivity pathways of molecules. Employing laser-induced spectroscopy has provided important results in recent years. These range from probing transition-state dynamics¹ to understanding the properties and effects of water solvation². These results are utilized to unravel how molecules and atoms, in different contexts, behave on a fundamental level upon laser-induced excitation. By leveraging this important experimental data with theoretical calculations, the underlying mechanisms affecting the chemical and physical behavior of molecules can be revealed. Herein, a variety of laser induced spectroscopy and dynamics techniques are employed to reveal the subtle interactions and peculiar dynamics of weakly-bound nitric oxide complexes and molecular systems.

1.1 Atmospheric and Combustion Relevance

Earth's climate is warming due to anthropogenic emissions of greenhouse gases, particularly carbon dioxide (CO₂), from fossil fuel combustion.³ However, anthropogenic emissions of non-CO₂ greenhouse gases, such as methane, nitric oxide and ozone-depleting substances, contribute significantly to global warming.³ Greenhouse gases (GHGs) alter Earth's climate by absorbing energy in the lower atmosphere and re-emitting it. The influence of emitted GHGs on future climate is estimated from the ability to absorb infrared radiation and its

persistence in the atmosphere.³ Since most anthropogenic emissions of these non-CO₂ GHGs are linked to society's fundamental needs for food and energy, these molecules will continue to be important to study due to their role in warming the climate.³⁻⁵

The troposphere is the region of the Earth's atmosphere in which we live and, in general, in which chemical compounds are emitted from anthropogenic processes.⁴ The emissions of oxides of nitrogen (NO), volatile organic compounds (VOCs), and hydrocarbons (alkanes) lead to a series of complex chemical and physical transformations.⁴ These transformations affect the formation of ozone in urban and regional areas, as well as, in the global troposphere, acid decomposition, and the formation of secondary particulate matter through gas/particle partitioning of both emitted chemical compounds and the atmospheric reaction products.^{4,6} Ozone, O₃, in the stratosphere absorbs ultraviolet radiation below 290 nm.⁶ Hence, only solar radiation of wavelength 290 nm and above is mostly transmitted through the stratospheric ozone layer and impacts the troposphere and the Earth's surface. Any depletion of stratospheric ozone allows shorter wavelength radiation to be transmitted through the stratosphere into the troposphere, leading to increased photodissociation rates in the troposphere, and still not fully understood effects on tropospheric chemistry.⁴ Therefore, the photochemistry of these anthropogenic species is important to investigate. Currently, there are large gaps in scientists' knowledge of NO's interactions with other atmospheric gases.

NO is an open-shell molecule which implies that it has an odd number of electrons, rendering NO a reactive radical. NO is emitted from soils and natural fires and is formed *in situ* in the troposphere from lightning.⁵ In addition, NO is emitted from combustion processes such as vehicle emissions and fossil-fueled power plants.⁴ In fact, fossil fuel combustion accounts for approximately 50% of the total emission of nitrogen oxides.⁴ Once NO is emitted naturally or anthropogenically, it behaves as a short-lived intermediate in a variety of chemical reactions in both the troposphere and the stratosphere.^{5,7} The atmospheric lifetime of NO ranges from <1 day to several days.⁵ Particularly in regions with high NO emissions from fossil-fuel combustion, complex photochemical processes involving NO and hydrocarbons (such as methane) result in photochemical smog with enhanced O₃ concentrations.⁸ Similar to NO, hydrocarbon concentrations have increased rapidly resulting from anthropogenic sources.⁹

Alkanes or hydrocarbons react with OH radicals, NO₃ radicals, and Cl atoms.^{7,10} The OH radical reaction is calculated to generally dominate as the main tropospheric loss process.⁹ Of the alkanes or hydrocarbons, methane is the most prominent in the atmosphere.¹⁰ Methane (CH₄) is emitted into the atmosphere from both biogenic and anthropogenic sources.⁴ Agriculture and fossil fuel exploitation together account for two-thirds of all human-derived CH₄ emissions, whereas a smaller fraction arises from waste treatment and biomass burning.³ At 1.8 ppm (as mole fraction in dry air), CH₄ is the most abundant non-CO₂ GHG in the atmosphere.³ Its present atmospheric mole fraction is 3 times

higher than observed in ice cores dated to 1300-1750 and is higher than that observed throughout the existing ice-core record.¹⁰ Methane has the second-largest global radiative forcing impact of anthropogenic greenhouse gases, but our understanding of its atmospheric chemistry is incomplete.¹⁰

As described, the increasing atmospheric concentrations of nitric oxide and methane are leading to complex chemical reactions and radiative impact that we do not fully understand. Additionally, NO and alkanes are prevalent in combustion environments where NO can be made from the catalytic reduction of N₂ and O₂. As such, there has previously been considerable interest in studying the chemical reactions of NO with other atmospheric species, including rare gas atoms, diatomics, and alkanes.¹¹⁻¹⁸ When these anthropogenically emitted species collide in the atmosphere, there is a transient moment at impact that the two collision partners may form a weakly-bound molecular complex or van der Waals complex.

Van der Waals molecules are weakly bound complexes of small atoms or molecules held together, not by chemical bonds, but by intermolecular attractions.¹⁹ These molecules, although weakly held together compared to chemical bonds, can exhibit unique properties than when they exist as individual partners.¹¹ The presence of these weakly bound complexes is expected whenever two molecules in the gas phase with low kinetic energy become trapped by their intermolecular attraction with each other.²⁰ How these weak interactions affect the dynamics of gas-phase complexes is not fully understood. Some Van der Waals complexes have even been known to experience the Jahn-

Teller effect, which carries with it its own peculiar dynamics (see Chapter 4). Therefore, the bimolecular collision dynamics of NO with alkanes in the atmosphere and combustion is of broad interest to the physical chemistry community.

1.2 Laser Spectroscopy

The advent of tunable lasers in the 1980s opened new opportunities to study molecules on a fundamental basis.²¹ They allowed for enhanced detection efficiencies and resonances to measure cross-sections, dynamics, total kinetic energy release and many other experimental quantities.²² Laser-based detection methods, such as laser-induced fluorescence (LIF) and later also resonance-enhanced multiphoton ionization (REMPI), allowed for the measurement of quantum-state-resolved cross-sections.²¹ The development of ion imaging and velocity map-imaging (VMI) techniques greatly enhanced the ability to record data that allows us to visualize the underlying chemistry at play in molecular species. The combination of laser-based ionization and ion imaging provides the revolutionary capability to create images of molecules that directly reflect the state-resolved energy partitioning from laser-initiated activation.²³ In recent decades, these improved detection techniques allowed for the study of a wide variety of systems. Ultimately the level of detail that can be reached in these experiments depends on the quality of the preparation and on the accuracy of product detection.

1.3 Scope of Thesis

The overall goal of this thesis is to understand the infrared-activated spectroscopy and dynamics of combustion- and atmospheric-related complexes. This thesis research has focused on the investigation of weakly bound van der Waals nitric oxide complexes present in the gas-phase. We achieve this goal using an array of laser spectroscopy and imaging techniques. This thesis provides a detailed description of these methods as well as their specific implementation through an in-depth analysis of the acquired results. Specifically, the vibrational spectroscopy of NO-CH₄ in the CH₄ asymmetric stretching region using resonant ion-depletion infrared spectroscopy and infrared action spectroscopy is presented, analyzed, and compared. Furthermore, we combine infrared activation of NO-CH₄ with velocity map imaging of NO ($X_2\Pi, v''=0, J'', F_n, \Lambda$) products to develop a molecular-level understanding of the nonreactive collisions of NO with CH₄. Finally, an outlook of our investigation into larger NO-alkane Van der Waals complexes is presented in the final chapter.

1.4 References

- (1) Babin, M. C.; DeWitt, M.; Lau, J. A.; Weichman, M. L.; Kim, J. B.; Song, H.; Guo, H.; Neumark, D. M. Observation of Resonances in the Transition State Region of the F + NH₃ Reaction Using Anion Photoelectron Spectroscopy. *Nat. Chem.* **2023**, *15* (2), 194–199. <https://doi.org/10.1038/s41557-022-01100-1>.
- (2) Zwier, T. S. Laser Spectroscopy of Jet-Cooled Biomolecules and Their Water-Containing Clusters: Water Bridges and Molecular Conformation. *J. Phys. Chem. A* **2001**, *105* (39), 8827–8839. <https://doi.org/10.1021/jp011659+>.
- (3) Montzka, S. A.; Dlugokencky, E. J.; Butler, J. H. Non-CO₂ Greenhouse Gases and Climate Change. *Nature* **2011**, *476* (7358), 43–50. <https://doi.org/10.1038/nature10322>.
- (4) Atkinson, R. Atmospheric Chemistry of VOCs and NO_x. *Atmos. Environ.* **2000**, *34* (12–14), 2063–2101. [https://doi.org/10.1016/S1352-2310\(99\)00460-4](https://doi.org/10.1016/S1352-2310(99)00460-4).
- (5) Bange, H. Chapter 2- Gaseous Nitrogen Compounds (NO, N₂O, N₂, NH₃) in the Ocean. In *Nitrogen in the Marine Environment*; Academic Press, 2008; pp 51–94. <https://doi.org/10.1016/B978-0-12-372522-6.00002-5>.
- (6) Liang, J.; Horowitz, L. W.; Jacob, D. J.; Wang, Y.; Fiore, A. M.; Logan, J. A.; Gardner, G. M.; Munger, J. W. Seasonal Budgets of Reactive Nitrogen Species and Ozone over the United States, and Export Fluxes to the Global Atmosphere. *J. Geophys. Res. Atmospheres* **1998**, *103* (D11), 13435–13450. <https://doi.org/10.1029/97JD03126>.
- (7) Tian, H.; Lu, C.; Ciais, P.; Michalak, A. M.; Canadell, J. G.; Saikawa, E.; Huntzinger, D. N.; Gurney, K. R.; Sitch, S.; Zhang, B.; Yang, J.; Bousquet, P.; Bruhwiler, L.; Chen, G.; Dlugokencky, E.; Friedlingstein, P.; Melillo, J.; Pan, S.; Poulter, B.; Prinn, R.; Saunio, M.; Schwalm, C. R.; Wofsy, S. C. The Terrestrial Biosphere as a Net Source of Greenhouse Gases to the Atmosphere. *Nature* **2016**, *531* (7593), 225–228. <https://doi.org/10.1038/nature16946>.
- (8) Kesik, M.; Ambus, P.; Baritz, R.; Brüggemann, N.; Butterbach-Bahl, K.; Damm, M.; Duyzer, J.; Horváth, L.; Kiese, R.; Kitzler, B.; Leip, A.; Li, C.; Pihlatie, M.; Pilegaard, K.; Seufert, S.; Simpson, D.; Skiba, U.; Smiatek, G.; Vesala, T.;

- Zechmeister-Boltenstern, S. Inventories of N₂O and NO Emissions from European Forest Soils. *Biogeosciences* **2005**, 2 (4), 353–375.
<https://doi.org/10.5194/bg-2-353-2005>.
- (9) Henze, D. K.; Seinfeld, J. H.; Ng, N. L.; Kroll, J. H.; Fu, T.-M.; Jacob, D. J.; Heald, C. L. Global Modeling of Secondary Organic Aerosol Formation from Aromatic Hydrocarbons: High- vs. Low-Yield Pathways. *Atmospheric Chem. Phys.* **2008**, 8 (9), 2405–2420. <https://doi.org/10.5194/acp-8-2405-2008>.
- (10) Schwietzke, S.; Sherwood, O. A.; Bruhwiler, L. M. P.; Miller, J. B.; Etiope, G.; Dlugokencky, E. J.; Michel, S. E.; Arling, V. A.; Vaughn, B. H.; White, J. W. C.; Tans, P. P. Upward Revision of Global Fossil Fuel Methane Emissions Based on Isotope Database. *Nature* **2016**, 538 (7623), 88–91.
<https://doi.org/10.1038/nature19797>.
- (11) Akiike, M.; Tsuji, K.; Shibuya, K.; Obi, K. Van Der Waals Vibrations of NO-Methane Complexes in the A₂Σ⁺ State. *Chem. Phys. Lett.* **1995**, 243 (1–2), 89–93. [https://doi.org/10.1016/0009-2614\(95\)00796-7](https://doi.org/10.1016/0009-2614(95)00796-7).
- (12) Crespo-Otero, R.; Suardiaz, R.; Montero, L. A.; García de la Vega, J. M. Potential Energy Surfaces and Jahn-Teller Effect on CH₄···NO Complexes. *J. Chem. Phys.* **2007**, 127 (10), 104305. <https://doi.org/10.1063/1.2752805>.
- (13) Holmes-Ross, H. L.; Gascooke, J. R.; Lawrance, W. D. Correlated Product Distributions in the Photodissociation of \tilde{A} State NO-CH₄ and NO-N₂ van Der Waals Complexes. *J. Phys. Chem. A* **2022**, 126 (43), 7981–7996.
<https://doi.org/10.1021/acs.jpca.2c06312>.
- (14) Potter, A. B.; Wei, J.; Reisler, H. Photoinitiated Predissociation of the NO Dimer in the Region of the Second and Third NO Stretch Overtones. *J. Phys. Chem. B* **2005**, 109 (17), 8407–8414. <https://doi.org/10.1021/jp046226w>.
- (15) Wen, B.; Meyer, H. The near IR Spectrum of the NO(XΠ₂)-CH₄ Complex. *J. Chem. Phys.* **2009**, 131 (3), 034304. <https://doi.org/10.1063/1.3175556>.
- (16) Wang, X.-D.; Robertson, P. A.; Cascarini, F. J. J.; Quinn, M. S.; McManus, J. W.; Orr-Ewing, A. J. Observation of Rainbows in the Rotationally Inelastic

Scattering of NO with CH₄. *J. Phys. Chem. A* **2019**, *123* (36), 7758–7767.
<https://doi.org/10.1021/acs.jpca.9b06806>.

(17) Tamé-Reyes, V. M.; Gardner, A. M.; Harris, J. P.; McDaniel, J.; Wright, T. G. Spectroscopy of the \tilde{A} State of NO–Alkane Complexes (Alkane = Methane, Ethane, Propane, and *n*-Butane). *J. Chem. Phys.* **2012**, *137* (21), 214307.
<https://doi.org/10.1063/1.4768811>.

(18) Potter, A. B.; Wei, J.; Reisler, H. Photoinitiated Predissociation of the NO Dimer in the Region of the Second and Third NO Stretch Overtones. *J. Phys. Chem. B* **2005**, *109* (17), 8407–8414. <https://doi.org/10.1021/jp046226w>.

(19) Ewing, G. E. Selection Rules for Vibrational Energy Transfer: Vibrational Predissociation of van Der Waals Molecules. *J. Phys. Chem.* **1987**, *91* (18), 4662–4671. <https://doi.org/10.1021/j100302a008>.

(20) Ewing, G. E. Selection Rules for Vibrational Energy Transfer: Vibrational Predissociation of van Der Waals Molecules. *J. Phys. Chem.* **1987**, *91* (18), 4662–4671. <https://doi.org/10.1021/j100302a008>.

(21) Levine, R. D. *Molecular Reaction Dynamics*; Cambridge University Press: Cambridge, 2009.

(22) Schafer, R.; Schmidt, P. Methods in Physical Chemistry. *Appl. Phys. Methods Inorg. Bioinorg. Chem.* **2007**, *1*.

(23) Whitaker, B. *Imaging in Molecular Dynamics: Technology and Applications*; Cambridge University Press: New York, 2003.

Chapter 2: Experimental Methods

2.1 Experimental Apparatus Description

To obtain fundamental information regarding the molecular level behavior of gas-phase species, a custom-built experimental apparatus was developed and utilized. A schematic describing the experimental apparatus is shown in Figure

2.1. The high-vacuum

apparatus consists of

two chambers

connected by a time-

of-flight (TOF) tube.

The individual

chambers are each

evacuated by their

respective mechanical

vacuum pumps

(Leybold, Trivac

D16B/D25B) as well

as turbo vacuum

pumps (Osaka,

TG390/TG900) to maintain operating vacuum pressures (10^{-5} - 10^{-6} torr).

Furthermore, each diffusion pump is outfitted with a oil mist eliminator to

condense pump oil and prevent diffusion into the chamber.

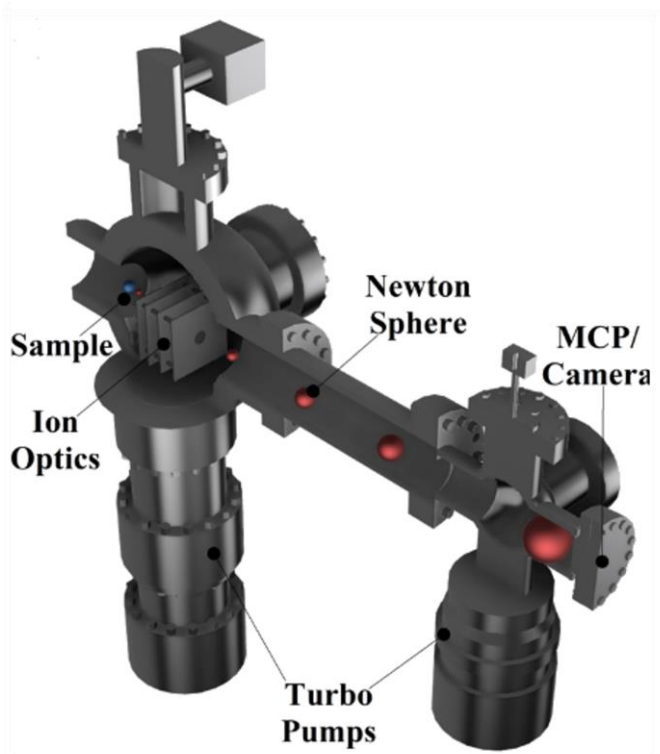


Figure 2.1. Schematic of the apparatus used to conduct the experiments. In each technique, the sample enters the apparatus on the left and travels to the right, where it impacts the MCP/camera detector.

The large chamber contains the sample inlet and therefore will be referred to as the source chamber. Whereas the second, smaller, chamber contains the detector and will be referred to as the detection chamber. The molecules are initially pulsed into the source chamber through the pulsed valve. The source chamber contains the sample inlet, two optical windows to allow laser radiation to enter, as well as an evacuation port which allows for the safe release of the vacuum when maintenance is necessary. In addition, the source chamber contains a set of ion optics which create an electric field in the chamber to accelerate photo-generated ions towards the detection chamber. Before any species can be investigated inside the experimental apparatus, we must achieve a certain amount of control over them.

2.2 Supersonic Jet Expansion

Supersonic jet expansion is leveraged to enhance the quality of the sample preparation; more specifically, to adiabatically cool the molecular species in question. To understand supersonic jet expansion, an overview of a pulse valve is described.

As illustrated in Figure 2.2, a specific mixture of gas is injected into the high-vacuum system utilizing a 500 μm pulse valve nozzle (Parker-Hannifin, Series 9, General Valve) operating at 10 Hz. The pulse valve is paramount to the experimental set up as it precisely releases the target gas into the chamber. The pulse valve consists of a faceplate containing the previously described orifice through which the gas flows. A Teflon (PTFE) poppet with a spring inside of a solenoid is pressed against the pulse valve orifice. The poppet is controlled and

pulses at a determined frequency by a digital delay generator (Quantum Composers, 9510+). Each cycle allows a pulse of gas into the chamber. Once the gas is pulsed through the orifice, it undergoes supersonic jet expansion.¹

As the gas molecules flow through the pulse valve, a molecular beam is created where the target molecule or molecular complex experiences a series of collisions with the inert carrier gas (Ar), adiabatically cooling the mixture down to low internal energies. The low temperature created by the collisions increases the speed of sound (a) through the molecular beam according to the equation $a = \sqrt{\gamma k_B / m}$.² In the equation, γ is the specific heat ratio, k_B is the Boltzmann constant, and m is the mass of the molecule. When the gas passes through the pulse valve, it has a high translational temperature due to the collisions, however the mass flow rate is very low.¹ As the mass flow rate increases and the collisional temperature decreases, the speed of sound also decreases. Once the flow rate matches and exceeds the speed of sound, the gas is said to be supersonic, which happens within a few millimeters as soon as the gas leaves the pulse valve into the chamber.²

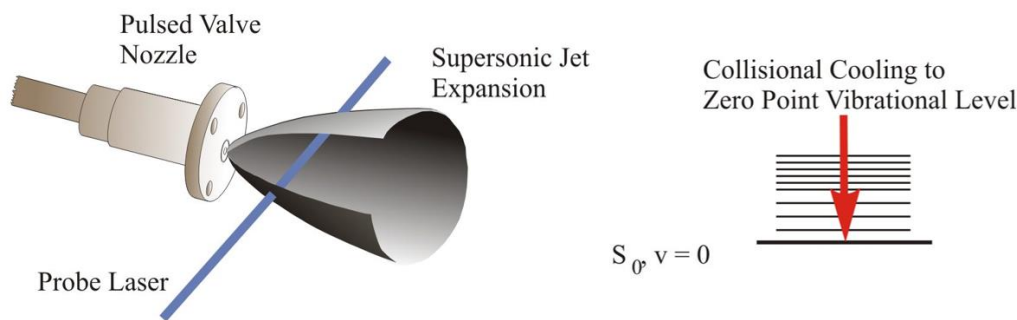


Figure 2.2. Schematic of the supersonic jet expansion and the generation of the molecular beam as it leaves the pulse valve into the source chamber, with the associated energy diagram of the adiabatic cooling.

After undergoing supersonic jet expansion, the coldest molecules are collected in the center of the molecular beam. Moving radially outward, the molecular beam contains more translationally excited molecules. At 30 mm from the pulsed valve nozzle, a skimmer (Boston Dynamics, 2mm orifice) is employed to select molecules with the lowest internal energy from the center of the molecular beam. The skimmer is effectively a reverse funnel with a hole facing the pulse valve and the open end facing into the vacuum chamber. The skimmer allows only the coldest molecules to proceed into the chamber, and the rest are removed. This allows for the preparation of species with their lowest vibrational and fewest rotational quantum states.^{1,2}

2.3 Laser Equipment and Methods

The generated cold samples from supersonic jet expansion are then interrogated with multiple two laser schemes. A Nd:YAG-pumped dye laser (Radiant Dyes, NarrowScan; 10 Hz) is utilized in tandem with a set of BBO crystals to produce tunable ultraviolet (UV) radiation to detect molecular

complexes or fragments following IR dissociation of the complex. The UV wavelengths are calibrated with a wavemeter (Coherent, WaveMaster). Furthermore, tunable IR radiation is generated with an optical parametric oscillator/amplifier (OPO/OPA LaserVision; 5 Hz), which is pumped by another Nd:YAG laser (Continuum Surelite II-10). The spatially overlapped IR and UV beams are aligned perpendicular to the cold molecular beam and both laser pulses are vertically polarized in the plane of the detector. There are a variety of techniques that can be executed utilizing this two laser pump-on pump-off set up which will be presented in section 2.3. Laser induced ionization of molecular complexes and their fragments is a powerful combination in tandem with mass spectroscopy.

2.3.1 Ion Optics and Detection Process

For the manipulation and control of the molecular complexes, time-of-flight mass spectroscopy is employed to extract subsequent information. Particularly, laser-induced spectroscopy techniques rely on the use of ion optics to directly map the velocity and angle distributions at which the ions travel to the detector.^{2,3} These ion optics are paramount to the time-of-flight experiments by establishing a constant electric field. This uniform electric field allows the mapping of the velocities and angular distributions onto the detector.³ Regardless of where in the laser interrogation region the ion is made, if it shares the same mass as the other ions in the region, they will be mapped onto the same position on the detector.³

The ion optic set-up in our experimental apparatus (Figure 2.1) contains three charged metal plates with varying sized circular holes and each with

specific voltages. The first metal plate is the repeller plate which is closest to the pulsed valve nozzle. The repeller plate also has the smallest hole and the largest voltage out of the three, 5000 V. The arrival timing of ions is inversely proportional to the voltage of the repeller plate. After the repeller plate, there are two extractor plates whose voltages aid in forming an electric field which has the optimal spatial resolution. The extractor plates, E1 and E2, have lower voltages than the repeller plate with each subsequent extractor plate decreasing in voltage. Their respective voltages are 4170 and 2200. The applied electric field is completed by the final metal plate which essentially acts as a grounding electrode. As a final note, the probe and pump lasers interrogate the molecular beam between the repeller plate and the first extractor plate. Therefore, after ionization or photodissociation, the ions are immediately accelerated toward the detector.

The applied electric field accelerates the ions downfield to a 40 mm diameter microchannel plate (MCP) detector. The electrical signal from these ions are interpreted by an oscilloscope (Teledyne LeCroy, Waverunner 8054) and by utilizing the electrical signal, the arrival times, and the applied electric field, the mass-to-charge ration (m/z) of the ions can be ascertained. Therefore, the electrical signal from these ions is utilized and manipulated in a variety of ways to extract information spectroscopically. Subsequent ion images are collected via the phosphorescent screen which is coupled to the MCP detector. The two-dimensional images of resulting product ion clouds are captured with a

charge coupled device (CCD). The varying data is collected using LabView 6 and is processed in Igor Pro 7 and pBASEX programs.

2.4 Spectroscopic Techniques

2.4.1 Resonant Two-Photon Ionization Spectroscopy

Resonant two-photon ionization (R2PI) is a one-laser experiment that is executed in tandem with the TOF mass spectrometer. Shown in Figure 2.3, the

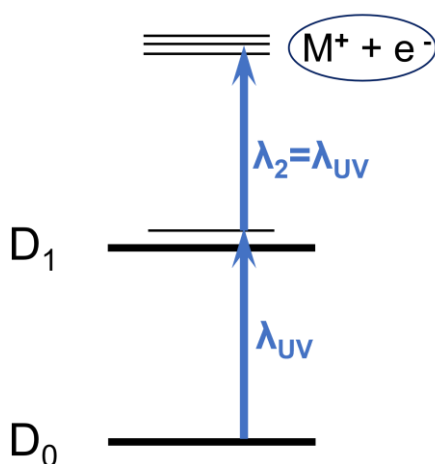


Figure 2.3. Schematic representation of resonant two-photon ionization.

technique is utilized to obtain electronically excited spectra of molecules and complexes using ultraviolet (UV) laser radiation. The spectra are generated by scanning the tunable UV radiation output of the probe laser, a Nd:YAG-pumped dye laser (Radiant Dyes, NarrowScan). When the UV wavelength (λ_{UV}) is resonant on a transition corresponding from the

ground electronic state to an excited vibronic state of a certain subset of the molecular species in the supersonic jet expansion, a UV photon is absorbed. Thereafter, a second photon of the same wavelength will ionize the molecules from the excited state to the ionization continuum. Therefore, when the tunable UV wavelength is resonant on a ground to excited state transition, there is an increase in the parent molecular ion signal detected by the TOF mass spectrometer. As such, as the parent molecular ion signal is monitored as a

function of the tunable UV wavelength, a vibrationally-resolved UV spectrum is obtained utilizing the LabView software. Figure 2.4 shows an example of an R2PI

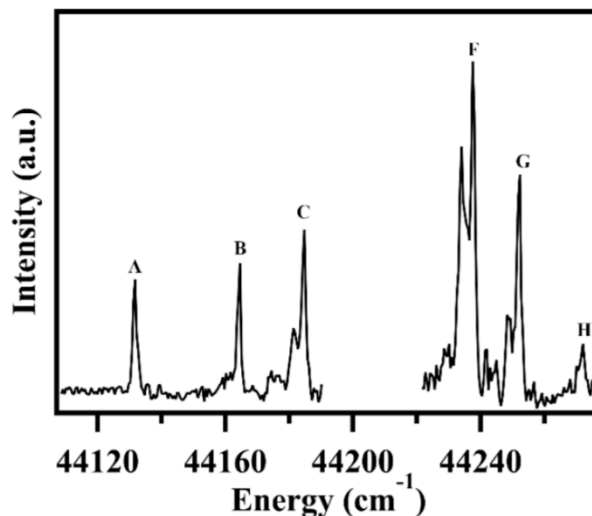


Figure 2.4. An example R2PI spectrum of the NO-CO complex with labelled vibronic transition peaks.

generated in our lab of the NO-CO complex. The product from R2PI is a vibrationally resolved UV spectrum of the molecular species in question. The R2PI spectrum can often comprise the sum of contributions arising from multiple conformational isomers. To disentangle such spectra, resonant ion-depletion infrared spectroscopy can be employed.

2.4.2 Resonant Ion-Dip Infrared Spectroscopy

Resonant ion-depletion infrared spectroscopy (RIDIRS) is a two-laser experiment depicted schematically in Figure 2.5 that is executed in tandem with the TOF mass spectrometer. This technique is utilized to obtain conformation-specific infrared spectra of molecular species. An R2PI spectrum, or electronic state transitions, is a pre-requisite to successfully perform this method since the excited state lifetime must be relatively long-lived. The probe laser is placed resonant on a ground to excited electronic state transition of the molecule, so a constant mass ion signal is monitored. Additionally, the IR laser or pump laser (OPO/OPA LaserVision) precedes the probe laser at a certain time, Δt (which

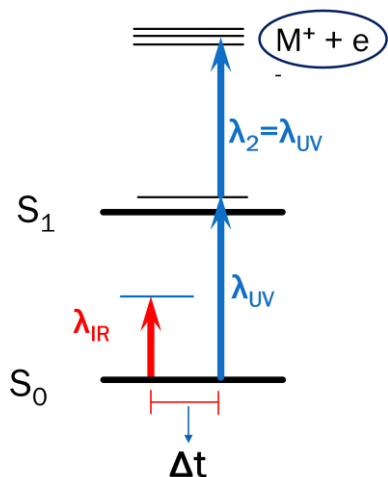


Figure 2.5. Schematic of resonant ion-depletion spectroscopy

varied on the order of 10-150 ns), and interrogates the molecular beam. The tunable IR radiation of the pump laser is scanned over a certain wavelength region. If an IR photon is absorbed by the molecular species, the molecular species is no longer able to be resonantly excited by the UV probe laser since the molecular species is now at a higher vibrational energy state.

Thus, the probed parent molecular ion signal will be depleted and is monitored as a function of the IR wavelength using the LabView software.

Utilizing LabView, two spectra are generated when monitoring the parent ion signal. The first spectrum results from monitoring the mass ion signal when it is resonantly excited by the UV probe laser. The second spectrum is generated

from monitoring the mass ion signal that results from infrared activation prior to resonant UV excitation. Both spectra are generated as the tunable IR energy scans a certain spectral region (typically 2800 – 3200 cm^{-1}). If the two spectra are subtracted, a difference spectrum is obtained, which represents the conformation-specific IR spectrum belonging to a certain conformational isomer. Thus, by changing the probe wavelength, different conformation-specific IR spectra can be recorded for each conformational isomer.

2.4.3 Infrared Action Spectroscopy

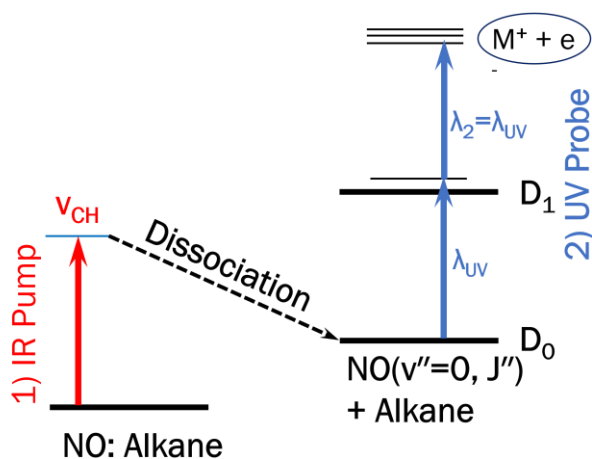


Figure 2.6. Schematic representation of infrared action spectroscopy.

Infrared action spectroscopy is an additional two laser experiment executed in tandem with a TOF mass spectrometer. Figure 2.6 shows that IR action spectroscopy is similar, in principle, to RIDIRS with a few important differences. In similar fashion,

the IR pump laser precedes the UV probe laser at a time, Δt . The tunable IR radiation is scanned over a certain wavelength region. If an IR photon is absorbed by the molecular species and is excited into a higher energy vibrational state, the bond dissociation energy is exceeded resulting in photodissociation of the molecular species. Therefore, the IR pump source will dissociate a molecular

complex to products that can be interrogated. The UV probe laser is used to monitor the products at a time Δt after the IR pump laser.

The UV probe laser is resonant on an electronic transition corresponding to a product ion species resulting from the dissociation of the parent molecular complex. This is an important distinction from RIDIRS where the UV probe laser is resonant on the ground to first excited electronic state transition of the parent molecular complex species. If the tunable IR wavelength is resonant on a transition which prompts dissociation of the molecular species, then a gain in product ion signal is observed. Thus, in this technique, the product ion signal is monitored as a function of the IR wavelength using LabView.

Utilizing LabView, two spectra are generated when monitoring the product ion signal. The first spectrum results from monitoring the background product ion signal when it is resonantly excited by the UV probe laser. The second spectrum is generated from monitoring the product ion signal that results from infrared activation (and dissociation) of the parent molecular complex prior to resonant UV excitation of the product ion. Both spectra are generated and monitored as a function of the tunable infrared wavelength. If the two spectra are subtracted, a difference spectrum is obtained. This difference spectrum represents the gain in product ions as a function of IR wavelength. By changing the UV probe wavelength to monitor different rovibronic states of the products, a wealth of information can be extracted on the products generated from infrared activation of the parent molecular complex. Therefore, this technique reveals information

about the formation of products and the relative energy partitioning into accessible quantized degrees of freedom.

2.4.4 Velocity-Map Imaging

Velocity map imaging (VMI) is a powerful technique which can measure the chemical reaction dynamics of molecular complexes. In particular, the photodissociation dynamics of complexes, the energy released to relative translation, and the internal energies of the co-fragments can be measured.

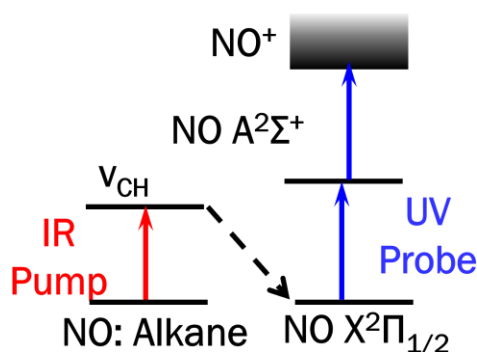


Figure 2.7. Schematic representation of velocity map imaging.

Shown in Figure 2.7, the VMI scheme is similar to the one described previously; however, this is a two-laser experiment. The first laser, the IR pump laser operating at 5 Hz, is fixed at a certain wavelength with sufficient energy to induce the photodissociation of the molecular complex in question. A counter-propagating probe laser, spatially overlapped and temporally following the photolysis laser by 50ns, monitors the formation of photofragments from decomposition of the complex. The pump laser is vertically polarized and aligns the complexes via interaction with their transition dipole moment, and then the complex decomposes to co-products. Following resonant ionization of products to cations, a three-dimensional Newton sphere is generated and accelerated by ion optics down the time-of-flight corridor and collide with the phosphorescent detector that illuminates when hit by ions (Figure 2.8). The CCD camera then

takes an image of this luminescence. By averaging the ion images, the angular and velocity distributions of the dissociation event can be determined.

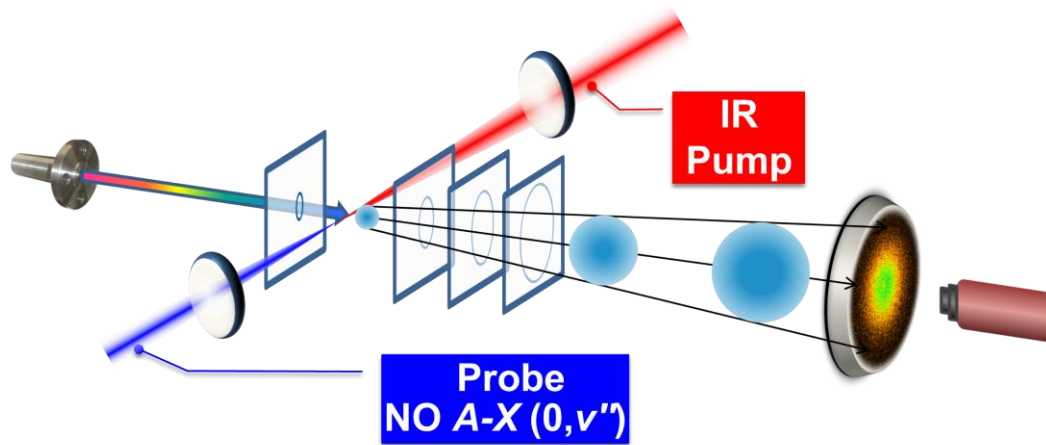


Figure 2.8. Path of the sample molecules in VMI, R2PI, RIDIRS, and IR action spectroscopy. Multicolored arrow represents cooling of the molecular beam as it approaches the laser radiation, and blue circles represent Newton spheres as they are accelerated toward MCP screen and CCD camera detector.

2.4.4.1 Newton Spheres, Total Kinetic Energy Release Distributions, and Beta Parameters

To understand the quantification of the data afforded by VMI, a description of a Newton sphere is needed. A Newton sphere is made up of the post-dissociation NO^+ cations recoiling from the center of mass in various directions with a speed of v , expanding as it passes through the chamber, until ultimately impacting the detector at the end, with a ring radius of $R = Nvt$, where t is the arrival time of the particles and N is the magnification factor of the.^{3,4} N was experimentally determined to be 1.31 for this chamber setup through calibration using O_2 photodissociation.^{5,6} Using $R = Nvt$, it is possible to determine the mass-weighted relative recoil velocity imparted to the co products (otherwise,

referred to as the total kinetic energy release) following photodissociation of the molecular complexes.⁷

In addition to obtaining the TKER distribution, the isotropy of the ion image is simultaneously measured. The ion image isotropy is dictated by the rate of the dissociation process.

If the dissociation occurs faster than the rotational period of the molecular species following

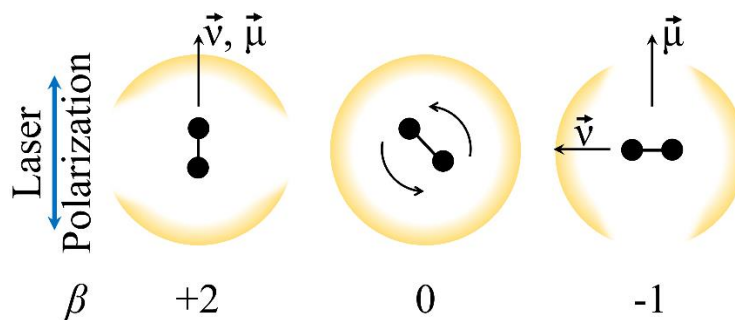


Figure 2.9. Diagram indicating the possible angular distributions and their corresponding anisotropy parameter, β .

excitation, then the

ions will be localized to the poles of the image ($\beta = -1$ or $+2$), whereas if the dissociation is slow, then there will be a more even radial distribution of the ions ($\beta = 0$).⁴ The anisotropy parameter β extracted from the ion images yields information on the dissociation time scale and relative orientation of the transition dipole moment, μ , with respect to the recoil velocity vector, v .⁴ In the limit that the anisotropy parameter $\beta = +2$, then the ground and excited electronic states share the same symmetry, whereas if $\beta = -1$, the electronic states have orthogonal symmetry.⁴

2.5 References

- (1) Smalley, R. E.; Wharton, L.; Levy, D. H. Molecular Optical Spectroscopy with Supersonic Beams and Jets. *Acc. Chem. Res.* **1977**, *10* (4), 139–145. <https://doi.org/10.1021/ar50112a006>.
- (2) Schafer, R.; Schmidt, P. Methods in Physical Chemistry. *Appl. Phys. Methods Inorg. Bioinorg. Chem.* **2007**, *1*.
- (3) Whitaker, B. *Imaging in Molecular Dynamics: Technology and Applications*; Cambridge University Press: New York, 2003.
- (4) Suits, A. G. Invited Review Article: Photofragment Imaging. *Rev. Sci. Instrum.* **2018**, *89* (11), 111101. <https://doi.org/10.1063/1.5045325>.
- (5) Blackshaw, K. J.; Quartey, N.-K.; Korb, R. T.; Hood, D. J.; Hettwer, C. D.; Kidwell, N. M. Imaging the Nonreactive Collisional Quenching Dynamics of NO ($A^2\Sigma^+$) Radicals with O₂ ($X^3\Sigma_g^-$). *J. Chem. Phys.* **2019**, *151* (10), 104304. <https://doi.org/10.1063/1.5109112>.
- (6) Blackshaw, K. J.; Ortega, B. I.; Quartey, N.-K.; Fritzeen, W. E.; Korb, R. T.; Ajmani, A. K.; Montgomery, L.; Marracci, M.; Vanegas, G. G.; Galvan, J.; Sarvas, Z.; Petit, A. S.; Kidwell, N. M. Nonstatistical Dissociation Dynamics of Nitroaromatic Chromophores. *J. Phys. Chem. A* **2019**, *123* (19), 4262–4273. <https://doi.org/10.1021/acs.jpca.9b02312>.
- (7) Dribinski, V.; Ossadtchi, A.; Mandelshtam, V. A.; Reisler, H. Reconstruction of Abel-Transformable Images: The Gaussian Basis-Set Expansion Abel Transform Method. *Rev. Sci. Instrum.* **2002**, *73* (7), 2634–2642. <https://doi.org/10.1063/1.1482156>.

Chapter 3: Infrared Spectroscopy of NO-CH₄

3.1 Introduction

Nitric oxide (NO) can be made from the catalytic reduction of N₂ and O₂ to NO/NO₂. This renders NO as a prevalent byproduct of many anthropogenic sources such as motor vehicles, industrial and commercial fuel combustion, and utilities. As such, there have been many studies performed on complexes of NO with rare gas atoms, diatomics, and alkanes (CH₄).¹⁻⁸ Methane (CH₄) is a potent greenhouse hydrocarbon and is the main component of natural gas. Most of the methane in the atmosphere derives from a range of human activities, such as extensive livestock farming, fossil fuel extraction, and combustion. Therefore, how NO and CH₄ interact in the atmosphere and combustion has been of interest. In this chapter, we aim to better understand the potential outcomes from bimolecular collisions involving NO and CH₄. Particularly, an understanding of the potential structure and lifetimes of this short-lived complex is needed.

The study of open-shell complexes is of far-reaching interest, as they are expected to exhibit interactions that are intermediate between van der Waals complexes and chemical bonding.¹ Open-shell reactive diatomic species, such as NO, permit access to a large intermolecular potential energy surface (IPS) and provide important spectroscopic information which can test the accuracy of predicted potential energy surfaces.¹ Of recent interest has been the study of NO with polyatomic partners. These systems often exhibit van der Waals interactions

and sometimes Jahn Teller (JT) distortions, such as NO-CH₄ as illustrated in Figure 3.1.²⁻⁴ These intermolecular interactions render the equilibrium geometry of NO-CH₄ difficult to determine. Previously, multiple experimental and computational studies have aimed at gaining an understanding of this complex.

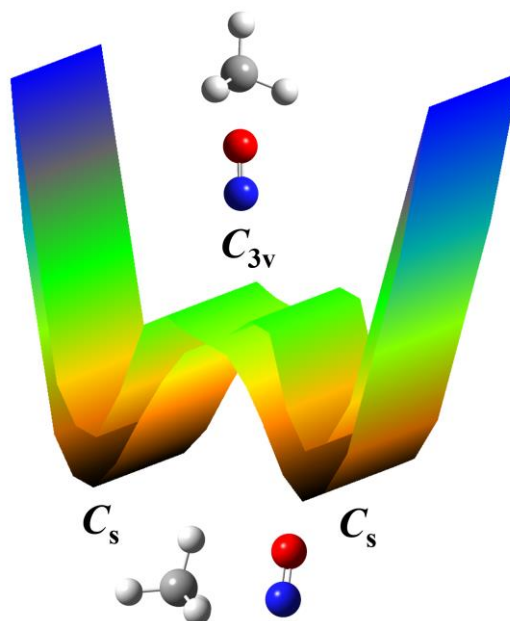


Figure 3.1. Schematic of the Jahn-Teller potential energy surfaces for the NO-CH₄ ground electronic states, adapted from Ref. 2. The internal rotation of either monomer results in a C_{3v} or C_s configuration. The lower and higher energy surfaces belong to the A'' and A' states, respectively, with C_s symmetry.

Akiike et al. were the first to report the A - X spectrum of NO:CH₄, using (1+1) resonance enhanced multiphoton ionization (REMPI), which exhibits repeating structures at low energy that become difficult to disentangle at higher energies.⁵ Wright *et al.* reported calculations at various levels of theory where the close-lying minima suggest large amplitude motion of the complex.^{4,6} Experimentally, the REMPI spectrum was concluded to be consistent with an effective C_{3v} geometry in both the ground (X) and first excited (A) electronic states.^{4,6} However, Crespo-Otero *et al.* determined through computational studies that NO-CH₄ is an effective JT distorted complex moving from C_s (Figure 3.1)

conformations through the C_{3v} complex.² Additionally, Wen and Meyer reported the NO overtone IR spectra of NO-CH₄ and concluded that the molecular complex spends most of its time in an orientation where NO is perpendicular to the face of CH₄ (C_s symmetry).³

Throughout these previous studies of NO-CH₄, it has become evident that this weakly bound molecular complex has complicated interactions which make the experimental data difficult to disentangle.^{2-4,6,7} Therefore, additional studies are needed to reveal how the different NO-CH₄ geometries contribute to the dissociation mechanisms. Therefore, in this chapter, we leverage resonant ion-depletion infrared spectroscopy and IR action spectroscopy in the fundamental CH₄ stretching region to characterize NO-CH₄ and its diverse set of intermolecular interactions.

3.2 Methods

Resonant ion-depletion infrared (RIDIR) spectroscopy and IR action spectroscopy experiments were performed in a differentially pumped molecular-beam apparatus described previously.⁸⁻¹⁰ A supersonic jet expansion was created by pulsing a gas mixture (1% nitric oxide (NO), 15% methane (CH₄), argon (Ar) balance) held at 5 bar through a 500 μ m pulse valve nozzle (Series 9, General Valve) into the high-vacuum chamber. Thus, NO-CH₄ molecular complexes were generated from adiabatic collisional cooling, and a skimmer (ID: 2mm, Beam Dynamics) placed approximately 30mm from the pulse valve nozzle was employed to select NO-CH₄ molecular complexes with the lowest internal energy from the molecular beam. A Nd:YAG-pumped dye laser (Radiant Dyes,

NarrowScan) was utilized in tandem with a set of BBO crystals to produce tunable ultraviolet (UV) radiation to detect NO-CH₄ molecular complexes or NO fragments following IR dissociation of the complex. Furthermore, tunable IR radiation was generated with an optical parametric oscillator/amplifier (OPO/OPA LaserVision), which was pumped by another Nd:YAG laser (Continuum Surelite II-10). The spatially overlapped IR and UV beams were aligned perpendicular to the molecular beam and both laser pulses were vertically polarized in the plane of the detector.

Isomer-specific RIDIR spectroscopy was carried out, wherein the UV laser was resonant on a specific $A \leftarrow X$ vibronic transition of a NO-CH₄ nuclear spin isomer. During experiments, the resonant UV wavelengths for NO-CH₄ were obtained with a wavelength meter (Coherent WaveMaster) and verified with previous results obtained by Wright and coworkers utilizing (1+1) resonance-enhanced multiphoton ionization (REMPI).^{4,6} The IR laser (5 Hz) preceded the UV laser (10 Hz) in time by 50 ns and was scanned across the CH stretch region from 2900 – 3200 cm⁻¹. When the scanned IR laser wavelength shares a common zero-point energy level as the probed NO-CH₄ nuclear spin isomer, the [NO-CH₄]⁺ mass ion signal was depleted and a difference spectrum was obtained with respect to the tunable IR wavelength using active baseline subtraction.

IR action spectra were collected by scanning the IR pump laser while the UV probe laser was fixed on specific rovibrational transitions of NO ($X^2\Pi$, $v''=0$, J'' , F_n , Λ) fragments generated from vibrational predissociation of the NO-CH₄ molecular complex. The spin-orbit (F_1 and F_2) and Λ -doublet ($\Pi(A'')$ and $\Pi(A')$)

levels were probed using the $Q_1(J'')$, $R_1(J'')$, $Q_2(J'')$, and $R_2(J'')$ lines. As the IR laser became resonant with a NO-CH₄ transition in the CH stretch region, signal gain in the NO⁺ mass ion channel was monitored from NO-CH₄ predissociation and averaged as a function of the IR wavelength.

3.3 Theoretical Calculations

To aid in characterizing NO-CH₄, a series of computational analyses were performed. Preliminary conformational searches were obtained to determine the most likely conformations of NO-CH₄. Electronic structure calculations for different NO-CH₄ conformational isomers were carried out using QChem 5.1¹¹ software and Gaussian 09¹². Using QChem software, conformational searches were carried out using unrestricted density functional theory at the ω b97XD/6-31G+(d,p) level of theory. Using this method, QChem will generate a list of possible isomers of the complex from an initial guess structure for a given level of theory. Therefore, four conformational searches were performed with four different, initial hypothesized structures.² These conformational searches obtained eight possible structures of NO-CH₄.

All eight structures geometries were subsequently optimized at varying levels of theory using Gaussian 09 and their harmonic vibrational frequencies were calculated. The same unrestricted-DFT at the ω b97XD/6-31G+(d,p) level of theory was utilized and six plausible structures were found. Subsequently, anharmonic vibrational frequencies of all six conformations were separately obtained using DFT at the ω B97X-D/6-311+G(3df,2p) level of theory. The conformations vary between C_{3v} and C_s similarly to the previous computational

studies. The C_{3v} conformations are such that NO is linear with respect to a C-H stretch of methane (Figure 3.2).

Two of the C_{3v} conformations are dependent on whether the nitrogen or oxygen of NO is oriented toward the face of methane (OC_{3v} and NC_{3v}). Two of the C_{3v} conformations are dependent on whether the nitrogen or oxygen of NO is

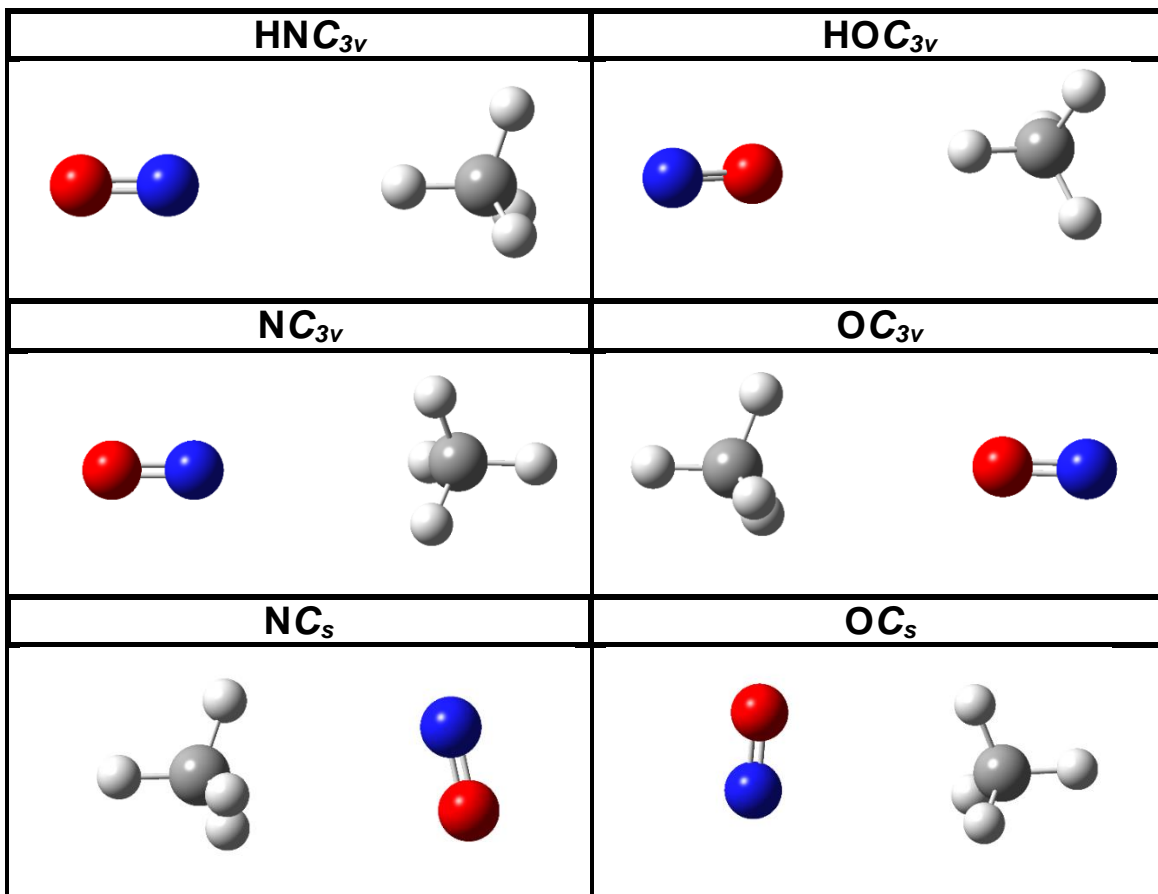


Figure 3.2. Optimized geometries and nomenclature of CH_3 face and CH bonded complexes with C_{3v} and C_s symmetries.

oriented toward the hydrogen of a C-H bond of methane (HOC_{3v} and HNC_{3v}).

The two C_s conformations are dependent on whether the nitrogen or oxygen of NO is leaning toward the face of methane (OC_s and NC_s). These calculations

were utilized to determine which conformational isomers are plausible in our experiments.

The weakly bound nature to NO-CH₄ made calculations difficult due to the relatively flat potential energy surface and relatively low barriers separating conformational isomers (< 50 cm⁻¹). Additionally, the simulated infrared spectra contained features that varied less than 4 cm⁻¹ depending on the conformation. As described previously, in-depth computational studies were previously carried out by Crespo-Otero et al.² Although these conformational searches are good predictions for experiments, the experimental data will be mainly compared to the computational work from Crespo-Otero et al.

3.4 Results

For the CH₄ component in the NO-CH₄ complex, symmetry and nuclear spin statistics involving the four equivalent hydrogen atoms have important effects on the spectra of methane-containing complexes. The rovibrational levels of CH₄ can have *A*, *F*, or *E* symmetry, reflecting the nuclear spin states.¹³ Due to the cold environment of the supersonic jet expansion, the NO-CH₄ complexes are plausibly formed mainly from NO and CH₄ monomers in their respective lowest-energy quantum levels. In particular, the primary contributions will originate from NO ($X^2\Pi_{1/2}$, $J''=0.5$) and CH₄ in its three lowest rotational energy levels corresponding to the *A*($J''=0$), *F*($J''=1$), and *E*($J''=2$) nuclear spin states having a relative population ratio of 5:9:2^{14,15}, respectively. Consequently, the *A*-, *F*-, and *E*-NO-CH₄ populations will plausibly reflect this ratio.

The resonant ion-depletion infrared (RIDIR) spectrum of NO-CH₄ (*m/z*=46) in the CH fundamental region over the 2950 – 3150 cm⁻¹ range is shown as the black trace in Figure 3.3. The UV laser was fixed on the transition assigned to the *F*-NO-CH₄ isomer by Wright and co-workers at 44,290.8 cm⁻¹. As seen in the figure, the transition band center at Q(1) in the RIDIR spectrum of NO-CH₄ is

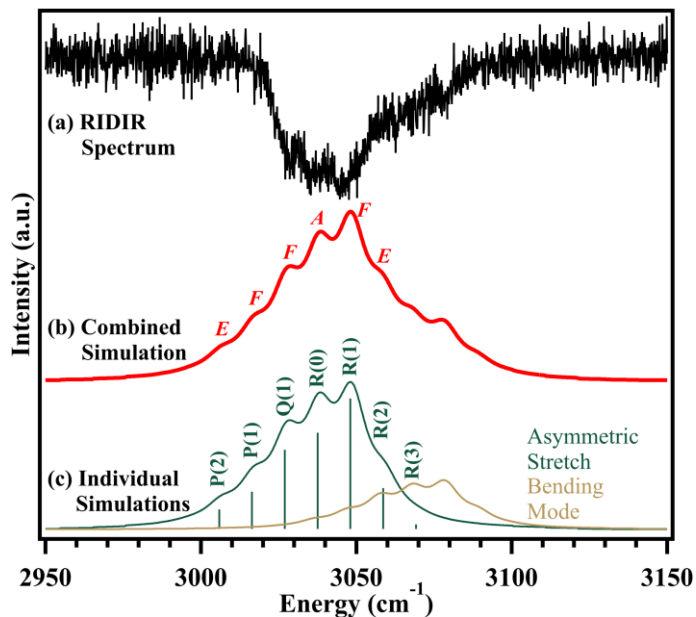


Figure 3.3. (a) Resonant ion-depletion infrared (RIDIR) spectrum of NO-CH₄ in the vicinity of the CH₄ stretch fundamental. (b, c) Combined and individual simulated IR spectra of the NO-CH₄ asymmetric CH stretch and bending rovibrational transitions assigned to the A, E, and F nuclear spin isomers.

located at ~3030 cm⁻¹ and is assigned to the asymmetric CH stretch. The basis of this assignment follows from the fact that no other features were observed at lower energy and that the spectral frequency of this band is consistent with a CH stretch transition. A weaker transition band is observed at approximately 30 cm⁻¹ to higher energy of the asymmetric CH stretch. This feature is attributed to a combination band involving simultaneous excitation of the asymmetric CH stretch and intermolecular bending mode (hindered internal rotation of the NO and/or CH₄ monomers). No other features are observed at higher energy.

Directly below the experimental RIDIR spectrum in Figure 3.3 is a simulation of the fundamental asymmetric CH stretch of the NO-CH₄ complex. The results are shown as the combined (red trace) and the individual components (green

and gold traces) for the asymmetric stretch and intermolecular bending mode. The rovibrational transition assignments belonging to the corresponding NO-CH₄ nuclear spin isomer are labeled in the figure. The simulated rovibrational spectrum was derived using CH₄ as the chromophore and was carried out using PGOPHER.¹⁶ The adjustable parameters included the ground and excited rotational constants (B'' and B' , respectively) of the asymmetric CH stretch of methane, the band origin (ν_0), the homogeneous Lorentzian broadening component of the spectral linewidth ($\Delta\nu_{\text{Lor}}/\text{cm}^{-1}$), and the rotational temperature (T_{rot}/K). The rotational temperature of *F*-NO-CH₄ complexes extracted from the IR spectrum simulation was found to be approximately 15 K, which is consistent with the $\sim 10\text{ cm}^{-1}$ zero-point energy of the *F*-NO-CH₄ isomer relative to the *A*-NO-CH₄ isomer.⁶ The agreement between the experimental and simulated IR spectra validates using methane as the chromophore and using the asymmetric stretch/intermolecular bending mode to model the NO-CH₄ vibrational transition. Additional RIDIR spectra of the *F*-, *A*-, and *E*-NO-CH₄ isomers are presented as well in Figure 3.3.

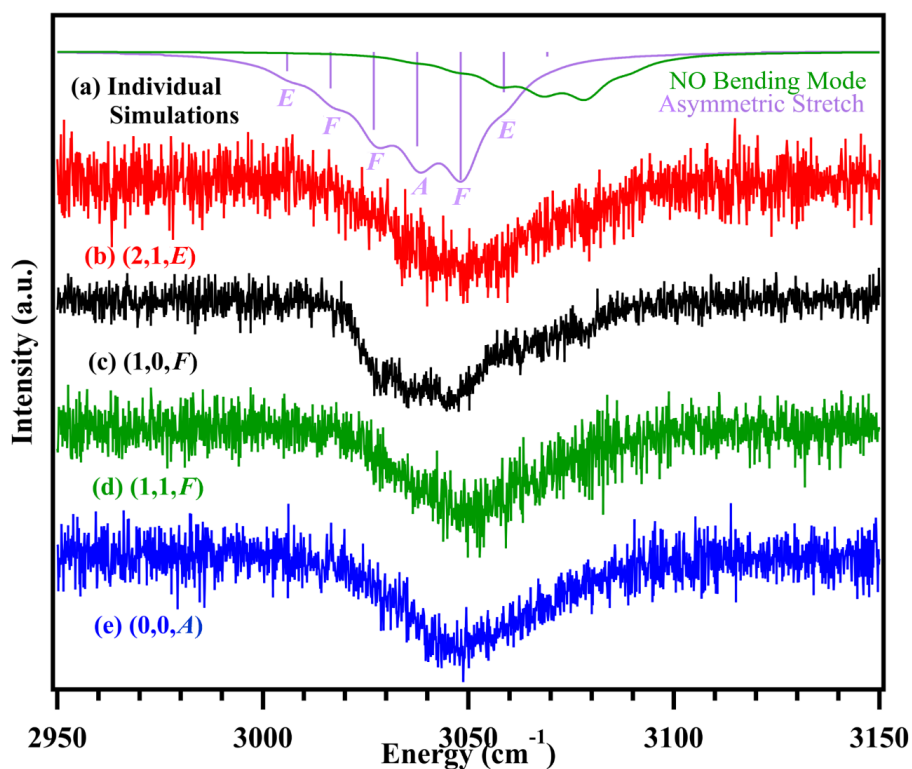


Figure 3.3. (a) Individual simulated IR spectra of the NO-CH₄ asymmetric CH stretch and bending rovibrational transitions assigned to the A, E, and F nuclear spin isomers. (b-e) Resonant ion-depletion infrared (RIDIR) spectra of NO-CH₄ in the vicinity of the CH₄ stretch fundamental.

The different RIDIR spectra in Figure 3.3 are generated by fixing the UV laser on transitions corresponding to the *F*-NO-CH₄, *E*-NO-CH₄, and *A*-NO-CH₄ isomers. These assignments are based off the fixed UV wavelengths compared to the resonant enhanced two-photon ionization (R2PI) spectrum obtained by Wright et al.^{15,17} The relative populations of the *A*(*J'*=0)-, *F*(*J'*=1)-, and *E*(*J'*=2)-NO-CH₄ nuclear spin isomer are expected to be 5:9:2. Therefore, the *A*-NO-CH₄ and *E*-NO-CH₄ are difficult to disentangle due to the relative low intensity of these populations owing to the decreased S/N as compared to the *F*-NO-CH₄ isomer.

Homogeneous linewidths extracted from experimental IR spectra are important parameters since they indicate the vibrational predissociation lifetime of the NO-CH₄ complex. A range of IR pulse energies was used to verify that the observed broadening of the spectral lines arises from rapid predissociation of NO-CH₄ and was not due to high IR power saturation broadening. Reducing the IR power from 6 mJ/pulse to 3 mJ/pulse was found to have no measurable effect on the spectral linewidth. From the simulated results, an upper limit for the lifetime broadening contribution to the spectral linewidth for the asymmetric CH stretch band was determined to be ~ 12 cm⁻¹, corresponding to a vibrationally excited state lifetime of approximately 440 fs for NO-CH₄.

In addition to recording the IR spectrum of NO-CH₄ using RIDIR spectroscopy, IR action spectroscopy was also carried out in the same spectral range. Here, IR activation of the NO-CH₄ complex resulted in NO photoproducts that were detected as a function of the IR wavelength. The IR action spectrum of NO-CH₄ in the asymmetric CH stretch region, detecting NO

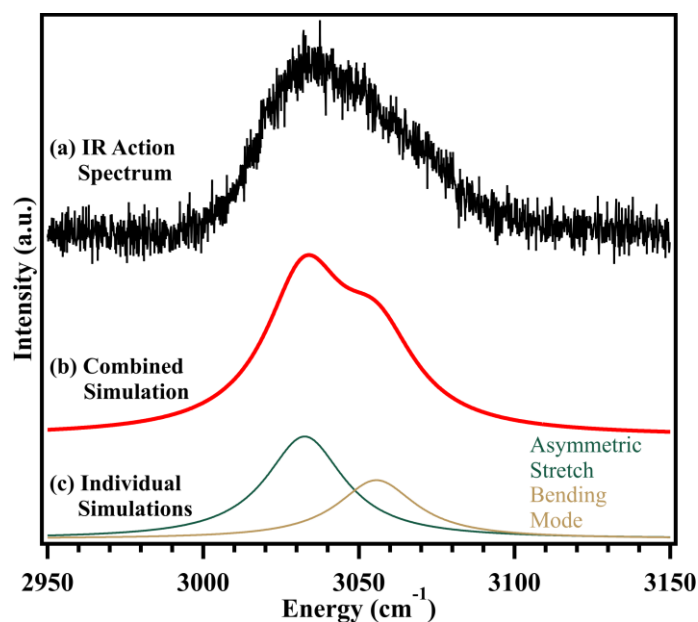


Figure 3.4. (a) Infrared action spectrum of NO-CH₄ obtained with the UV probe laser fixed on the NO (*A-X*(0,0) *R*₁(10.5)) transition while scanning the IR pump laser frequency across the CH stretch region. (b,c) Combined and individual simulated IR spectra of the NO-CH₄ asymmetric CH stretch and bending rovibrational transitions.

($X^2\Pi$, $v''=0$, $R_1(J''=10.5)$) products is shown in Figure 3.4. The IR action spectrum resembles the spectral energy range as the RIDIR spectrum, albeit with an increased spectral linewidth. This is plausibly due to the fact that in the RIDIR spectroscopy method, the IR spectrum is obtained by depleting a small subset of the NO-CH₄ rotational population since the UV probe laser is resonant solely on the *F*-NO-CH₄ nuclear spin isomer. However, when performing IR action spectroscopy, the IR pump laser activates all NO-CH₄ nuclear spin isomers, leading to the observed NO product signal. The peak of the IR action spectrum is also located at 3030 cm⁻¹ and the spectrum extends to approximately 3100 cm⁻¹, which is attributed to the asymmetric CH stretch/intermolecular bending combination band. Directly below the IR action spectrum in Figure 3.4 are the combined and individual IR simulations using a similar procedure as described above. However, the rotational temperature and the Lorentzian broadening components used were 3 K and 24 cm⁻¹, respectively. The rotational temperature for the simulations was varied with the 12 cm⁻¹ Lorentzian broadening value used for the RIDIR spectrum, but the simulated IR spectra results were inconsistent with the experimental IR spectrum. Accordingly, the vibrational predissociation lifetime of the asymmetric CH stretch is approximately 220 fs, which is in agreement with that determined using RIDIR spectroscopy.

3.5 Discussion

Owing to the cold conditions inherent in the adiabatic cooling environment of the supersonic jet expansion, the relative populations of the *A*($J''=0$)-, *F*($J''=1$)-, and *E*($J''=2$)-NO-CH₄ nuclear spin isomer are expected to be 5:9:2, respectively.

The asymmetric CH stretch of the CH₄ chromophore is a triply degenerate vibrational mode with *F* symmetry, which is broken by the weak intermolecular coordination of NO with the CH₄ monomer. This likely leads to a complex rotational energy level pattern and corresponding IR spectrum for NO-CH₄. The rovibrational assignments for the NO-CH₄ IR spectrum are provided in Figure 3.3 and are compared with spherical top simulations for CH₄ using PGOPHER.¹⁶ Transitions between rotational levels of the CH₄ monomer with different symmetry is forbidden, resulting in the $A \leftrightarrow A$, $F \leftrightarrow F$, and $E \leftrightarrow E$ selection rule for nuclear spin isomer transitions. The allowed IR transitions for the *A*-NO-CH₄ isomer terminate only on $J''=1$ rotational levels in the vibrationally excited asymmetric CH stretch state. Thus, only the single R(0) rovibrational band arises from the *A* isomer in the IR spectrum of NO-CH₄. Furthermore, transitions due to the *F*-NO-CH₄ isomer can only access $J''=0, 1$, and 2 rovibrational asymmetric CH stretch levels, corresponding to the P(1), Q(1), and R(1) transition bands. Though the nuclear spin population ratio is larger for the *F* isomer compared to *A*, the relative peak intensities of the *F* isomer are expected to be smaller since there are more allowed $F \leftrightarrow F$ transitions available. Lastly, the *E*-NO-CH₄ isomer transitions access the $J''=1, 2$, and 3 only, giving rise to the P(2), Q(2), and R(2) bands. Since the RIDIR spectrum in Figure 3.3 was collected using the UV transition for the *F*-NO-CH₄ isomer, the IR spectrum likely reflects a rovibrational intensity pattern with greater relative population for the *F* isomer. This is due to the fact that the *F*-NO-CH₄ isomer zero-point energy is $\sim 10 \text{ cm}^{-1}$ above the *A* isomer,⁶ which is equivalent to the $\sim 15 \text{ K}$ rovibrational temperature used in the IR

spectroscopy simulations. However, the IR action spectrum in Figure 3.4 shows the R(0) rovibrational band has the largest relative intensity, in agreement with the 5:9:2 (*A:F:E*) nuclear spin population ratio and with the expectation that transitions arising from the *A* isomer are the most intense.

Previously, Meyer and co-workers reported the near IR spectrum of NO-CH₄ in the first vibrational NO overtone region.³ The spectral linewidths of the transitions indicated a vibrational predissociation lifetime (τ_{vp}) of about 100 ps. From Figures 3.3 and 3.4, the Lorentzian line broadening used to obtain excellent agreement between the experimental and simulated IR spectra of NO-CH₄ indicated a vibrational predissociation lifetime (τ_{vp}) of approximately 200-400 fs. Therefore, we conclude that activation of the asymmetric CH stretch is more directly coupled to the intermolecular modes of the complex (including the reaction coordinate) via intramolecular vibrational redistribution compared to the NO stretch. Similarly, the asymmetric CH stretch transition ($\tau_{vp} < 5$ ps) for the OH-CH₄ complex was significantly more broadened compared to the fundamental ($\tau_{vp} \sim 38$ ps) and overtone ($\tau_{vp} \sim 25$ ps) OH stretches.^{14,18} Furthermore, the ~ 11 cm⁻¹ blue spectral shift of the NO-CH₄ asymmetric stretch spectrum with respect to the CH₄ monomer (3019 cm⁻¹) indicates there is a more repulsive interaction and correlated change in the intermolecular potential brought about by excitation of the asymmetric CH stretching motion. Equivalently, the ~ 11 cm⁻¹ blue frequency shift represents a corresponding decrease in the τ_{vp} ^{19,20} predicted to be approximately 300 fs, in agreement with the lifetime determined from the IR spectral linewidths.

Furthermore, Meyer et al³ observed a shoulder transition band due to NO hindered rotation built off of the NO overtone origin transition of NO-CH₄. The authors concluded that the spacing and relative intensities of these two bands were consistent with a NO-CH₄ geometry where NO is oriented perpendicular to the intermolecular axis for a considerable amount of time. This is consistent with a C_s configuration attributed to Jahn-Teller distortion from C_{3v} symmetry structures and is in agreement with the calculated geometry in Figure 3.1. Using calculations at the RCCSD(T)/aug-cc-pVTZ level, Crespo-Otero and co-workers² determined that NO-CH₄ is a dynamic Jahn-Teller distorted complex from the potential energy surfaces arising from eight complex isomer geometries, with NO interacting with either the CH₄ face or C-H bond. For the C_{3v} geometries, the nitrogen or oxygen atom of NO is oriented toward the CH₄ face or C-H bond, whereas rotation of NO leads to C_s configurations with NO perpendicular to the face or C-H bond of CH₄. The stabilization due to Jahn-Teller distortion is greatest for the NO-CH₄ face geometries with C_{3v} symmetry, generating two C_s states with A' and A'' symmetry having calculated dissociation energies (*D*₀) of 100 and 140 cm⁻¹, respectively.² Crespo-Otero determined that the NO-CH₄ system is expected to easily transition between the A' and A'' surfaces. Furthermore, from analysis of the two-dimensional potential energy surface of the NO-CH₄ face complexes, the zero-point energy is near the barriers between the C_s and C_{3v} configurations. The authors, therefore, concluded that the NO-CH₄ system is affected by a dynamic Jahn-Teller effect. The Jahn-Teller and

vibrational predissociation dynamics imprinted on the co-products is the focus of the next chapter.

3.6 Conclusion

Herein, we have reported the vibrational spectroscopy of the bimolecular collision complex between nitric oxide and methane (NO-CH₄). We recorded the resonant ion-depletion infrared spectra and infrared action spectra of NO-CH₄ in the CH₄ antisymmetric stretching region, which reveal a significantly broad spectrum centered at 3030 cm⁻¹ and extends over 50 cm⁻¹. The vibrational structure of the infrared spectra can be explained by CH₄ internal rotation and assignment of transitions involving three different nuclear spin isomers of CH₄. The infrared spectra also show extensive homogenous broadening due to prompt vibrational predissociation of NO-CH₄.

Although NO-CH₄ has been investigated using electronic excitation, there has been little work on its infrared activation. NO-CH₄ exhibits interactions that are suggest possible JT effects.^{2,3} Therefore, how the dynamics of this system evolve over the bimolecular collision coordinate is of interest. Thus, in Chapter 4 we aim to reveal the dynamics of the system that sensitively depend on subtle JT interactions. NO-CH₄ offers the unique opportunity to investigate how JT effects impact not only the equilibrium geometry of JT systems, but also the peculiar dynamics they carry with them.

3.7 References

- (1) Potter, A. B.; Wei, J.; Reisler, H. Photoinitiated Predissociation of the NO Dimer in the Region of the Second and Third NO Stretch Overtones. *J. Phys. Chem. B* **2005**, *109* (17), 8407–8414. <https://doi.org/10.1021/jp046226w>.
- (2) Crespo-Otero, R.; Suardiaz, R.; Montero, L. A.; García de la Vega, J. M. Potential Energy Surfaces and Jahn-Teller Effect on CH₄···NO Complexes. *J. Chem. Phys.* **2007**, *127* (10), 104305. <https://doi.org/10.1063/1.2752805>.
- (3) Wen, B.; Meyer, H. The near IR Spectrum of the NO($\chi\Pi_2$)–CH₄ Complex. *J. Chem. Phys.* **2009**, *131* (3), 034304. <https://doi.org/10.1063/1.3175556>.
- (4) Tamé-Reyes, V. M.; Gardner, A. M.; Harris, J. P.; McDaniel, J.; Wright, T. G. Spectroscopy of the \tilde{A} State of NO–Alkane Complexes (Alkane = Methane, Ethane, Propane, and *n*-Butane). *J. Chem. Phys.* **2012**, *137* (21), 214307. <https://doi.org/10.1063/1.4768811>.
- (5) Akiike, M.; Tsuji, K.; Shibuya, K.; Obi, K. Van Der Waals Vibrations of NO–Methane Complexes in the A₂ Σ^+ State. *Chem. Phys. Lett.* **1995**, *243* (1–2), 89–93. [https://doi.org/10.1016/0009-2614\(95\)00796-7](https://doi.org/10.1016/0009-2614(95)00796-7).
- (6) Musgrave, A.; Bergeron, D. E.; Wheatley, R. J.; Wright, T. G. Electronic Spectroscopy of the Deuterated Isotopomers of the NO-methane Molecular Complex. *J. Chem. Phys.* **2005**, *123* (20), 204305. <https://doi.org/10.1063/1.2125748>.
- (7) Holmes-Ross, H. L.; Gascooke, J. R.; Lawrance, W. D. Correlated Product Distributions in the Photodissociation of \tilde{A} State NO–CH₄ and NO–N₂ van Der Waals Complexes. *J. Phys. Chem. A* **2022**, *126* (43), 7981–7996. <https://doi.org/10.1021/acs.jpca.2c06312>.
- (8) Blackshaw, K. J.; Quartey, N.-K.; Korb, R. T.; Hood, D. J.; Hettwer, C. D.; Kidwell, N. M. Imaging the Nonreactive Collisional Quenching Dynamics of NO ($A^2\Sigma^+$) Radicals with O₂ ($X^3\Sigma_g^-$). *J. Chem. Phys.* **2019**, *151* (10), 104304. <https://doi.org/10.1063/1.5109112>.
- (9) Blackshaw, K. J.; Ortega, B. I.; Quartey, N.-K.; Fritzeen, W. E.; Korb, R. T.; Ajmani, A. K.; Montgomery, L.; Marracci, M.; Vanegas, G. G.; Galvan, J.;

Sarvas, Z.; Petit, A. S.; Kidwell, N. M. Nonstatistical Dissociation Dynamics of Nitroaromatic Chromophores. *J. Phys. Chem. A* **2019**, *123* (19), 4262–4273. <https://doi.org/10.1021/acs.jpca.9b02312>.

(10) Pan, C.; Zhang, Y.; Lee, J. D.; Kidwell, N. M. Imaging the Dynamics of CH₂BrI Photodissociation in the Near Ultraviolet Region. *J. Phys. Chem. A* **2018**, *122* (15), 3728–3734. <https://doi.org/10.1021/acs.jpca.7b12268>.

(11) Shao, Y.; Gan, Z.; Epifanovsky, E.; Gilbert, A. T. B.; Wormit, M.; Kussmann, J.; Lange, A. W.; Behn, A.; Deng, J.; Feng, X.; Ghosh, D.; Goldey, M.; Horn, P. R.; Jacobson, L. D.; Kaliman, I.; Khaliullin, R. Z.; Kuś, T.; Landau, A.; Liu, J.; Proynov, E. I.; Rhee, Y. M.; Richard, R. M.; Rohrdanz, M. A.; Steele, R. P.; Sundstrom, E. J.; Woodcock, H. L.; Zimmerman, P. M.; Zuev, D.; Albrecht, B.; Alguire, E.; Austin, B.; Beran, G. J. O.; Bernard, Y. A.; Berquist, E.; Brandhorst, K.; Bravaya, K. B.; Brown, S. T.; Casanova, D.; Chang, C.-M.; Chen, Y.; Chien, S. H.; Closser, K. D.; Crittenden, D. L.; Diedenhofen, M.; DiStasio, R. A.; Do, H.; Dutoi, A. D.; Edgar, R. G.; Fatehi, S.; Fusti-Molnar, L.; Ghysels, A.; Golubeva-Zadorozhnaya, A.; Gomes, J.; Hanson-Heine, M. W. D.; Harbach, P. H. P.; Hauser, A. W.; Hohenstein, E. G.; Holden, Z. C.; Jagau, T.-C.; Ji, H.; Kaduk, B.; Khistyayev, K.; Kim, J.; Kim, J.; King, R. A.; Klunzinger, P.; Kosenkov, D.; Kowalczyk, T.; Krauter, C. M.; Lao, K. U.; Laurent, A. D.; Lawler, K. V.; Levchenko, S. V.; Lin, C. Y.; Liu, F.; Livshits, E.; Lochan, R. C.; Luenser, A.; Manohar, P.; Manzer, S. F.; Mao, S.-P.; Mardirossian, N.; Marenich, A. V.; Maurer, S. A.; Mayhall, N. J.; Neuscamman, E.; Oana, C. M.; Olivares-Amaya, R.; O'Neill, D. P.; Parkhill, J. A.; Perrine, T. M.; Peverati, R.; Prociuk, A.; Rehn, D. R.; Rosta, E.; Russ, N. J.; Sharada, S. M.; Sharma, S.; Small, D. W.; Sodt, A.; Stein, T.; Stück, D.; Su, Y.-C.; Thom, A. J. W.; Tsuchimochi, T.; Vanovschi, V.; Vogt, L.; Vydrov, O.; Wang, T.; Watson, M. A.; Wenzel, J.; White, A.; Williams, C. F.; Yang, J.; Yeganeh, S.; Yost, S. R.; You, Z.-Q.; Zhang, I. Y.; Zhang, X.; Zhao, Y.; Brooks, B. R.; Chan, G. K. L.; Chipman, D. M.; Cramer, C. J.; Goddard, W. A.; Gordon, M. S.; Hehre, W. J.; Klamt, A.; Schaefer, H. F.; Schmidt, M. W.; Sherrill, C. D.; Truhlar, D. G.; Warshel, A.; Xu, X.; Aspuru-Guzik, A.; Baer, R.;

Bell, A. T.; Besley, N. A.; Chai, J.-D.; Dreuw, A.; Dunietz, B. D.; Furlani, T. R.; Gwaltney, S. R.; Hsu, C.-P.; Jung, Y.; Kong, J.; Lambrecht, D. S.; Liang, W.; Ochsenfeld, C.; Rassolov, V. A.; Slipchenko, L. V.; Subotnik, J. E.; Van Voorhis, T.; Herbert, J. M.; Krylov, A. I.; Gill, P. M. W.; Head-Gordon, M. Advances in Molecular Quantum Chemistry Contained in the Q-Chem 4 Program Package. *Mol. Phys.* **2015**, *113* (2), 184–215.

<https://doi.org/10.1080/00268976.2014.952696>.

(12) Frisch, M. J.; Trucks, G.; Schlegel, H. B.; Scuseria, G. E.; Robb, M. A.; Cheeseman, J. R. Gaussian 09, 2009.

(13) Bunker, P. R.; Jensen, P. *Molecular Symmetry and Spectroscopy*, 2nd ed.; NRC Research Press: Ottawa, Canada, 1998.

(14) Wheeler, M. D.; Tsiouris, M.; Lester, M. I.; Lendvay, G. OH Vibrational Activation and Decay Dynamics of CH₄–OH Entrance Channel Complexes. *J. Chem. Phys.* **2000**, *112* (15), 6590–6602. <https://doi.org/10.1063/1.481232>.

(15) Musgrave, A.; Bergeron, D. E.; Wheatley, R. J.; Wright, T. G. Electronic Spectroscopy of the Deuterated Isotopomers of the NO-methane Molecular Complex. *J. Chem. Phys.* **2005**, *123* (20), 204305.

<https://doi.org/10.1063/1.2125748>.

(16) Western, C. M.; Billinghurst, B. E. Automatic and Semi-Automatic Assignment and Fitting of Spectra with PGOPHER. *Phys. Chem. Chem. Phys.* **2019**, *21* (26), 13986–13999. <https://doi.org/10.1039/C8CP06493H>.

(17) Tamé-Reyes, V. M.; Gardner, A. M.; Harris, J. P.; McDaniel, J.; Wright, T. G. Spectroscopy of the \tilde{A} State of NO–Alkane Complexes (Alkane = Methane, Ethane, Propane, and *n*-Butane). *J. Chem. Phys.* **2012**, *137* (21), 214307.

<https://doi.org/10.1063/1.4768811>.

(18) Tsiouris, M.; Wheeler, M. D.; Lester, M. I. Activation of the CH Stretching Vibrations in CH₄–OH Entrance Channel Complexes: Spectroscopy and Dynamics. *J. Chem. Phys.* **2001**, *114* (1), 187–197.

<https://doi.org/10.1063/1.1328747>.

(19) Miller, R. E. *The Vibrational Spectroscopy and Dynamics of Weakly Bound Neutral Complexes* | *Science*.

<https://www.science.org/doi/10.1126/science.240.4851.447> (accessed 2022-12-29).

(20) Le Roy, R. J.; Davies, M. R.; Lam, M. E. Rate Proportional to (Frequency Shift)² and Other “All Else Being Equal” Correlations in Vibrational Predissociation. *J. Phys. Chem.* **1991**, *95* (6), 2167–2175.

<https://doi.org/10.1021/j100159a018>.

Chapter 4: Infrared Activated Dynamics of NO-CH₄

4.1 Introduction

The structure and properties of molecular systems are determined by the motion of its electrons and nuclei and by their interaction.¹ However, the quantum-mechanical treatment of the molecular structure is normally carried out using a few simplifying approximations, the most common being the adiabatic approximation.² The adiabatic approximation implies that the large difference between the masses of the electron and nucleus causes a significant difference in their velocities of motion.¹ Thus, for every instantaneous nuclear configuration, there exists a stationary distribution of the electronic cloud (electronic state).² It is clear that this approximation takes a more classical approach to the quantum-mechanical role of the electrons in the nuclear dynamics. However, this assumption enables the solving of the Schrödinger equation in two stages and with much more ease. There are many cases of systems which deviate from the adiabatic approximation. One of the most fascinating deviations from the adiabatic approximation in modern physics and chemistry is the Jahn-Teller (JT) effect.

In 1934, two famous physicists, L. Landau and E. Teller, developed the idea of the spontaneous distortion of the nuclear configuration in an orbitally degenerate electronic term formed by two or more orbital states with the same energy.^{1,2} This resulted in the JT theorem which is now widely used in research on the structure and properties of polyatomic systems. In fact, JT theory is an approach to the general understanding of the properties of molecules and

crystals, which is in principle applicable to any system with more than two atoms.¹ The JT effect applies to a range of important applications including spectroscopy, stereochemistry, and structural phase transitions. The JT effect also is the basis of many important discoveries including the high-temperature superconductor, whose discoverers explain that “the guiding idea in developing this concept was influenced by the Jahn-Teller polaron model.”¹ The JT effect has also been instrumental in explaining the properties of a novel class of compounds, the fullerenes, and it is employed in emerging areas of chemical reactivity mechanisms.¹⁻⁶

In the presence of the JT effect, the electrons do not adiabatically follow the motions of the nuclei, and the nuclear states are determined not only by the averaged field of the electrons, but also by the details of the electronic structure and their changes under nuclear displacements.¹ The influence of these nuclear displacements (vibrations) via electron-vibrational (vibronic) interactions is considered a perturbation to the degenerate states, and only linear terms of this vibronic coupling of the electronic states to the nuclear displacements are taken into account.² Therefore, the JT theorem is based on a perturbational group-theoretical analysis of the behavior of adiabatic potential energy surfaces of polyatomic systems near the point of electronic degeneracy.²

Jahn and Teller examined all types of degenerate terms of all symmetry point groups. They showed that for any orbital degenerate term of any molecular system, there are non-totally symmetric displacements with respect to which the adiabatic potential energy surface of the electronic term has no minimum (however, molecules with linear arrangements of atoms are exceptions).^{1,2,5} The lack of a minimum of the adiabatic potential energy surface at the point of electronic degeneracy is often interpreted as instability of the nuclear configuration, which leads to its real (observable) spontaneous distortion that removes the electronic degeneracy.¹⁻⁶ This spontaneous distortion lowers the overall energy of the

system as it evolves from a higher symmetry configuration to a lower symmetry configuration, as can be seen in Figure 4.1.

Here, Na_3 distorts from a higher symmetry D_{3h} configuration to either an acute or obtuse C_{2v}

configuration.⁵ Thus, lowering the symmetry and

equivalently lowering the

overall energy of the system in the process.

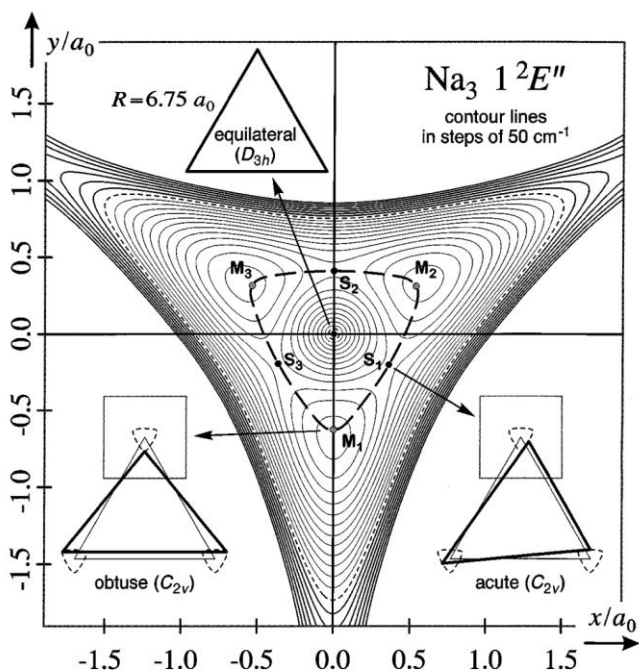


Figure 4.1. A classic example of a JT distortion. A cut through the lower adiabatic PES of the electronic A state of Na_3 for E mode atomic displacements, adapted from Ref. 5.

The JT theorem, and derivatives of it, have been instrumental in explaining the observed physical and chemical behavior of trigonal molecular systems (X_3 , AB_3 , etc.), distorted tetrahedral and square-planar systems (X_4 , MX_4 , cyclobutadiene, etc.), benzene and cyclopentane families, and a wide array of solid-state systems.¹⁻⁶ However, there is still a gap in scientists' knowledge about how the JT effect manifests in weakly-bound complexes such as NO-CH₄. As described previously, there has been previous computational and experimental evidence suggesting that NO-CH₄ is a JT distorted complex (Figure 4.2).⁷ These subtle JT interactions are responsible for complicating the vibrational spectroscopy of the complex. Additionally, how the JT distortion affects the energy partitioning to products and the dissociation dynamics is not understood. Therefore, understanding the dynamics following IR activation of NO-CH₄ would aid in revealing the energy exchange mechanisms from bimolecular collisions involving NO and CH₄. This is due to the fact that the NO-CH₄ complex is an intermediate along the potential energy surface of a

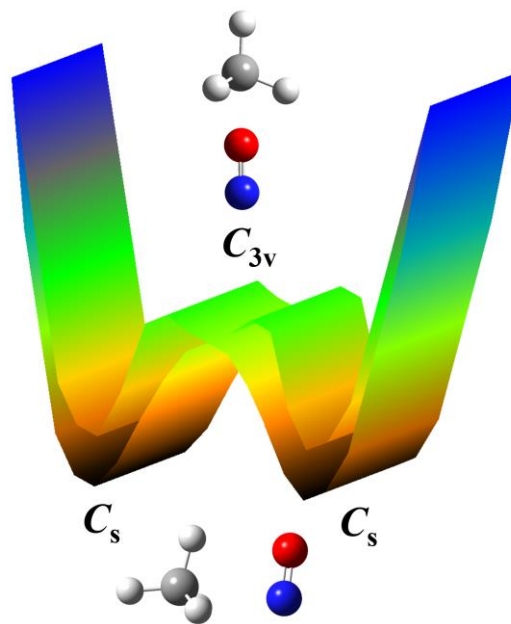


Figure 4.2. Schematic of the Jahn-Teller potential energy surfaces for the NO-CH₄ ground electronic states, adapted from Ref. 7. The internal rotation of either monomer results in a C_{3v} or C_s configuration. The lower and higher energy surfaces belong to the A'' and A' states, respectively, with C_s symmetry.

NO + CH₄ bimolecular collision. A similar methodology was utilized in the rigorous studies of a related molecular complex, OH-CH₄.⁸⁻¹⁰

Lester et al. published a series of papers investigating the activation and decay dynamics of OH-CH₄ in the OH overtone and fundamental stretching region, as well as the CH₄ fundamental stretching region.⁸⁻¹⁰ Focusing on the latter, the OH-CH₄ complex was studied in the CH₄ symmetric and antisymmetric stretching regions (ν_1 and ν_3).⁹ The OH-CH₄ experimental spectra exhibited extensive homogeneous broadening which corresponded to lifetimes of 38 and 24 ps for OH-CH₄ prepared with either one quanta or two quanta of OH stretch, respectively.⁹ Following infrared excitation, OH-CH₄ was found to have a short vibrational predissociation lifetime due to near resonant vibration-to-vibration (V-V) energy transfer from the OH monomer to stretching and bending levels of the CH₄ partner.^{8,9} The OH ($\nu=0,1$) product state distributions following vibrational predissociation of the OH-CH₄ exhibit a strong propensity for forming OH fragments with very little rotational excitation.^{8,9} The slight differences in the exact rotational level OH populates in either $\nu=0$ or $\nu=1$ depends on the available energy and the vibrational mode of methane which causes the dominant V-V energy pathway.⁸⁻¹⁰ OH-CH₄ serves as a model system to build on and understand the NO-CH₄ collision complex in more detail.

Although NO-CH₄ has been investigated using electronic excitation, there has been little work on its infrared activation. NO-CH₄ exhibits interactions that are not present in OH-CH₄ such as possible JT effects.^{7,11} Therefore, how the dynamics of this system compare to OH-CH₄ is an intriguing proposition. Thus,

we aim to reveal the dynamics of the system that sensitively depend on subtle JT interactions. NO-CH₄ offers the unique opportunity to investigate how JT effects impact not only the equilibrium geometry of JT systems, but also the peculiar dynamics they carry with them. Therefore, we have leveraged an array of spectroscopic techniques to gain insights into the possible JT dynamics at play in this molecular complex. Ultimately, we have gained insights into the mode-specific energy transfer pathways following fragmentation of the NO-CH₄ molecular complex, which reveals the nonreactive energy exchange mechanisms of NO and CH₄ collisions in the atmosphere and high-energy environments.

4.2 Experimental Methods

Velocity map imaging (VMI) experiments were performed in a differentially pumped molecular-beam apparatus described previously.^{12–14} A supersonic jet expansion was created by pulsing a gas mixture (1% nitric oxide (NO), 15% methane (CH₄), argon (Ar) balance) held at 5 bar through a 500 μm pulse valve nozzle (Series 9, General Valve) into the high-vacuum chamber. Thus, NO-CH₄ molecular complexes were generated from adiabatic collisional cooling, and a skimmer (ID: 2mm, Beam Dynamics) placed approximately 30mm from the pulse valve nozzle was employed to select NO-CH₄ molecular complexes with the lowest internal energy from the molecular beam. A Nd:YAG-pumped dye laser (Radiant Dyes, NarrowScan) was utilized in tandem with a set of BBO crystals to produce tunable ultraviolet (UV) radiation to detect NO fragments following IR dissociation of the complex. Furthermore, tunable IR radiation was generated with an optical parametric oscillator/amplifier (OPO/OPA LaserVision), which was

pumped by another Nd:YAG laser (Continuum Surelite II-10). The spatially overlapped IR and UV beams were aligned perpendicular to the molecular beam and both laser pulses were vertically polarized in the plane of the detector.

To reveal the vibrational predissociation outcomes following IR activation of NO-CH₄ molecular complexes, VMI experiments were carried out under the same experimental conditions as the infrared spectroscopy studies (Chapter 3). Here, the translational and angular distributions of NO ($X^2\Pi$, $v''=0$, J'' , F_n , Λ) products from IR fragmentation of the NO-CH₄ molecular complexes were detected. The IR pump laser was resonant with a NO-CH₄ transition while the UV laser was fixed on specific rovibrational transitions of NO ($X^2\Pi$, $v''=0$, J'' , F_n , Λ) fragments generated from vibrational predissociation of the NO-CH₄ molecular complex. The spin-orbit (F_1 and F_2) and Λ -doublet ($\Pi(A'')$ and $\Pi(A')$) levels were probed using the $Q_1(J'')$, $R_1(J'')$, $Q_2(J'')$, and $R_2(J'')$ lines.

The NO⁺ ions generated with the probe laser were accelerated on axis with the supersonic jet expansion using a stack of ion optic plates and velocity-focused onto a position-sensitive multichannel plate/phosphor screen detector, which was gated for the NO⁺ mass ($m/z=30$). A charge-coupled device (CCD) camera captured spatial ion images of the three-dimensional NO product ion cloud. The resonant IR wavelengths spanned different features in the IR action spectrum, and the ion images were collected in an active baseline subtraction fashion. Using the pBASEX¹⁵ program, 3D reconstruction extracts the anisotropy parameter, β . Furthermore, the ion images were analyzed with pBASEX to determine the velocity distributions of the NO ($v'' = 0$, J'') products. This was

accomplished by implementing an inverse Abel transformation along the vertical axis and subsequently integrating the radial distributions over the polar angle. Using conservation of momentum, the total kinetic energy released (TKER) to NO + CH₄ is obtained.

Additionally, we directly probed the populations of NO rotational levels ($X^2\Pi$, $v''=0$, J'' , F_n , Λ) to generate product state distributions (PSDs). As previously described, the R2PI scheme ionizes the specific NO ($X^2\Pi$, $v''=0$, J'' , F_n , Λ) product, thus enabling state-specific measurements. To obtain PSDs, the tunable IR radiation resonantly excites NO-CH₄ with the wavelength corresponding to the most prominent feature in the IR action spectrum at 3045 cm⁻¹. The UV probe laser wavelength is altered to different rotational transitions of NO $X^2\Pi$ and $A^2\Sigma^+$ using LIFBASE¹⁶ program. As a note, the IR pump laser precedes the UV probe laser similar to the VMI experiments. For these studies, we probed Q₁, R₁, Q₂, and R₂ of NO products, with varying rotational levels J'' detected. The intensities of the probed rotational levels are found by integrating the area of the NO⁺ mass ion signal in the TOF spectrum. Each intensity is averaged over three different measurements. The averaged area is then corrected for several experimental conditions through the following equation:

$$I(J) = \ln \left[\frac{A}{(2J + 1)(P * l)} \right]$$

Here, $I(J)$ is the corrected intensity value for a specific NO rotational state, which takes into account the power of the laser (P), the Honl-London line strength of the transition (l), and the degeneracy of the rotational level, $2J + 1$. To quantify the NO

product population following IR-induced fragmentation of NO-CH₄, $I(J)$ is plotted with the respect to the energy of the NO rotational level, thus generating a product state distribution.

4.3 Results

The ion images of select NO ($X^2\Pi$, $v''=0$, $R_1(J'')$) products from IR activation of NO-CH₄ at 3045 cm⁻¹ are shown as insets in Figure 4.3. As observed in the figure, the anisotropy of the ion image features depends sensitively on the rotational quantum number, $R_1(J'')$. Also presented in Figure 4.3, the total kinetic energy release (TKER) distributions for NO + CH₄ co-products are obtained using conservation of momentum. The translationally slow component peak in the TKER distributions reaches a maximum at approximately 225 cm⁻¹, whereas the translationally fast component with its largest intensity at ~1400 cm⁻¹ increasingly becomes more prominent for $R_1(J'')>6.5$. Furthermore, the translationally slow component also increases in intensity for $R_1(J'')>6.5$. Shown in Figure 4.4 are the ion images and TKER distributions for NO ($X^2\Pi$, $v''=0$,

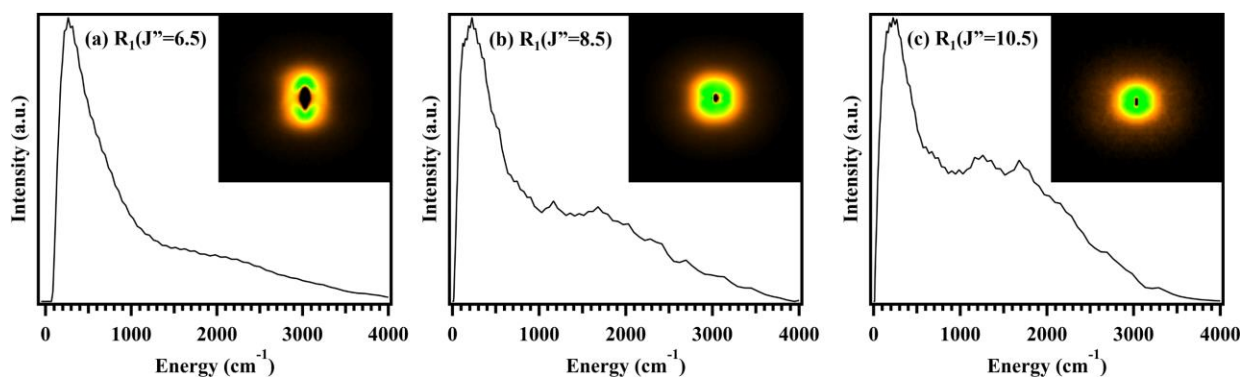


Figure 4.3. Total kinetic energy release (TKER) of NO ($X^2\Pi$, $v''=0$, $R_1(J'')$) and CH₄ products from IR activation of NO-CH₄ complexes. The insets show the experimental ion images, revealing features with anisotropic and isotropic distributions for (a) $R_1(J'')=6.5$, (b) $R_1(J'')=8.5$, and (c) $R_1(J'')=10.5$. The IR pump laser is parallel to the detector plane.

$Q_1(J'')$ fragments from IR activation of NO-CH₄ at 3045 cm⁻¹, displaying similar resemblance to the R-branch results.

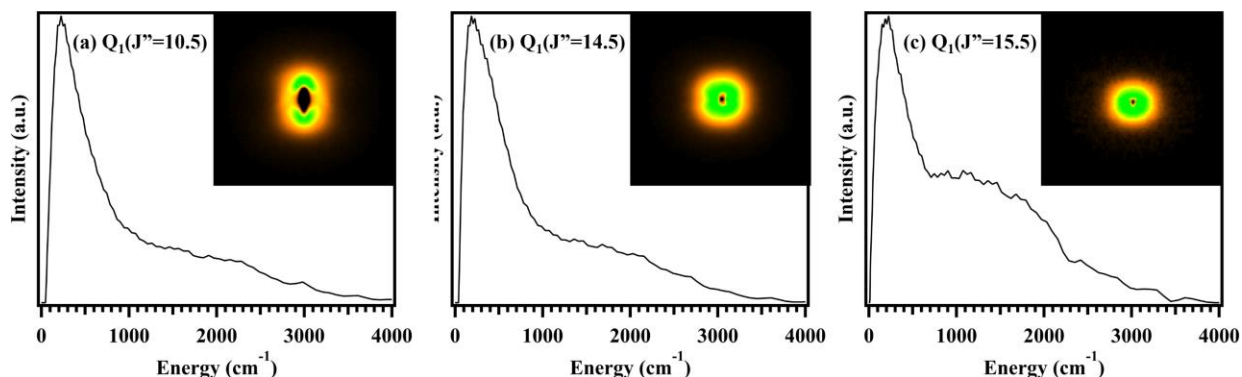


Figure 4.4. Total kinetic energy release (TKER) of NO ($X^2\Pi$, $v''=0$, $Q_1(J'')$) and CH₄ products from IR activation of NO-CH₄ complexes. The insets show the experimental ion images, revealing features with anisotropic and isotropic distributions for (a) $Q_1(J''=10.5)$, (b) $Q_1(J''=14.5)$, and (c) $Q_1(J''=15.5)$. The IR pump laser is parallel to the detector plane.

The ion images of select $R_2(J'')$ and $Q_2(J'')$ levels for NO ($X^2\Pi$, $v''=0$) products from IR activation of NO-CH₄ at 3045 cm⁻¹ are shown in Figures 4.5 and 4.6. As also observed in the figures, the anisotropy of the ion image features

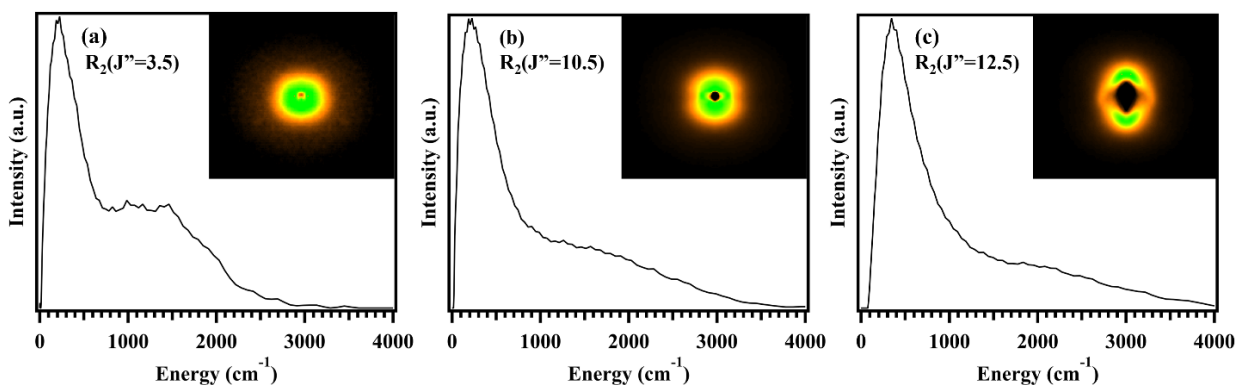


Figure 4.5. Total kinetic energy release (TKER) of NO ($X^2\Pi$, $v''=0$, $R_2(J'')$) and CH₄ products from IR activation of NO-CH₄ complexes. The insets show the experimental ion images, revealing features with anisotropic and isotropic distributions for (a) $R_2(J''=3.5)$, (b) $R_2(J''=10.5)$, and (c) $R_2(J''=12.5)$. The IR pump laser is parallel to the detector plane.

depends sensitively on the rotational quantum number, $R_2(J'')$. The TKER

distributions for NO + CH₄ co-products were obtained as described previously and bear similar resemblance to the R₁(J'') and Q₁(J'') results for NO ((X₂Π, v''=0) products. A similar trend continues such that the anisotropic ion images are accompanied by predominantly the low TKER feature, whereas isotropic ion images are accompanied by the additional broad peak at higher TKER.

When employing linearly polarized radiation, the angular distribution can

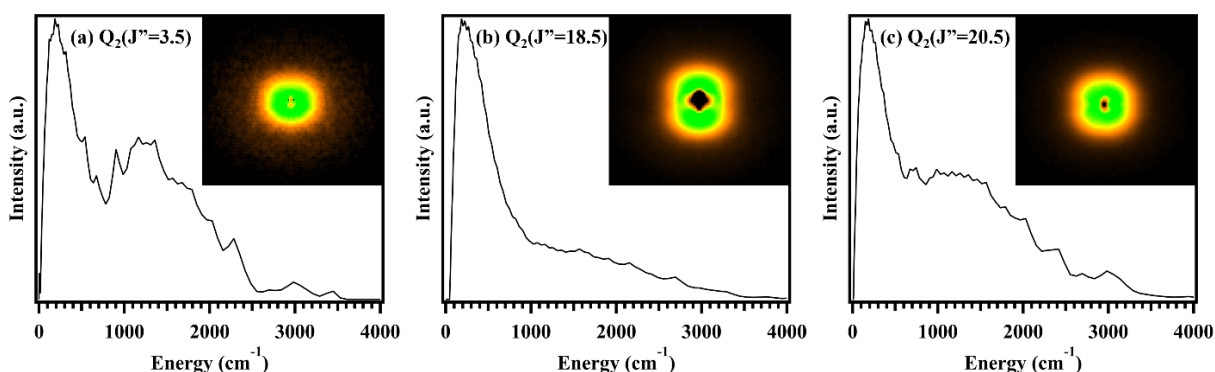


Figure 4.6. Total kinetic energy release (TKER) of NO ($\chi^2\Pi$, $v''=0$, $Q_2(J'')$) and CH₄ products from IR activation of NO-CH₄ complexes. The insets show the experimental ion images, revealing features with anisotropic and isotropic distributions for (a) $Q_2(J''=3.5)$, (b) $Q_2(J''=18.5)$, and (c) $Q_2(J''=20.5)$. The IR pump laser is parallel to the detector plane.

be extracted quantitatively from ion images by converting the laboratory frame to the molecular frame distribution with $I(\theta) \sim 1 + \beta \cdot P_2(\cos \theta)$. In this expression, θ is the angle between the fragment velocity vector and light polarization direction, and P_2 is a second-order Legendre polynomial. From 3D image reconstruction using pBASEX¹⁵, the anisotropy parameter β for the translationally slow component is approximately +0.83 for all J'' and $\beta \sim 0$ for the translationally fast feature of the ion image. Thus, we tentatively conclude that the ion images are a combination of a translationally slow, anisotropic feature with a translationally fast, isotropic component appearing as J'' changes. All NO product ion images

contain a dominant anisotropic feature, which is consistent with NO-CH₄ vibrational predissociation occurring on a faster time scale compared to its rotational period ($\tau < 2.5$ ps).

4.3.1 Product State Distributions

The product state distributions of NO ($X^2\Pi$, $v''=0$, $R_1(J'')$, $R_2(J'')$, $Q_1(J'')$, $Q_2(J'')$) are displayed in Figures 4.7 – 4.10. The NO probe signal intensity was integrated three separate times from following IR activation of the NO-CH₄ complex. The intensity is corrected as described in the methods and is plotted against the internal energy of NO ($X^2\Pi$, $v''=0$, J'').

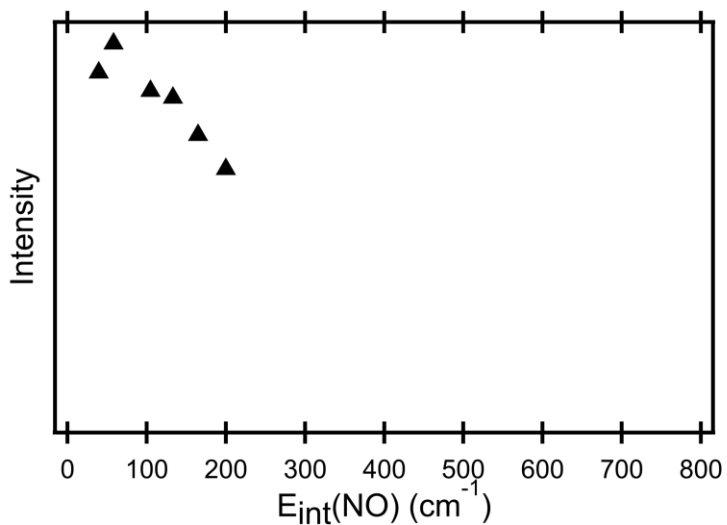


Figure 4.7. Product state distributions of NO ($X^2\Pi$, $v''=0$, $R_1(J'')$) products from IR activation of NO-CH₄ complexes. IR activation energy of 3045 cm^{-1} .

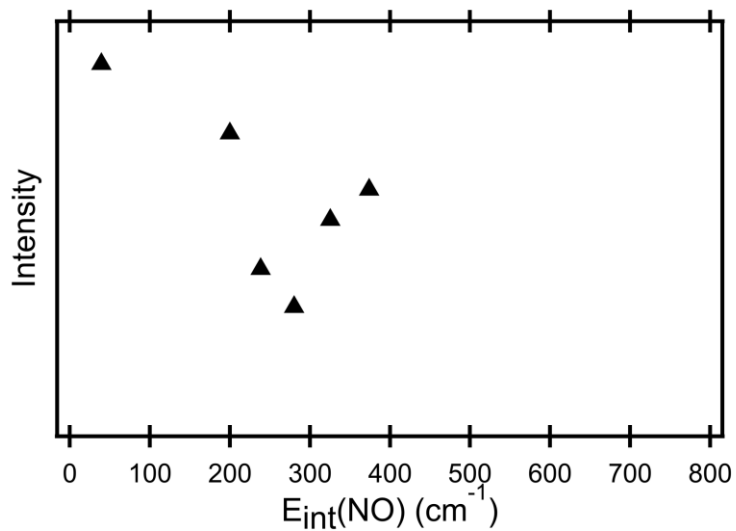


Figure 4.8. Product state distributions of NO ($X^2\Pi$, $v''=0$, $R_2(J'')$) products from IR activation of NO-CH₄ complexes. IR activation energy of 3045 cm⁻¹.

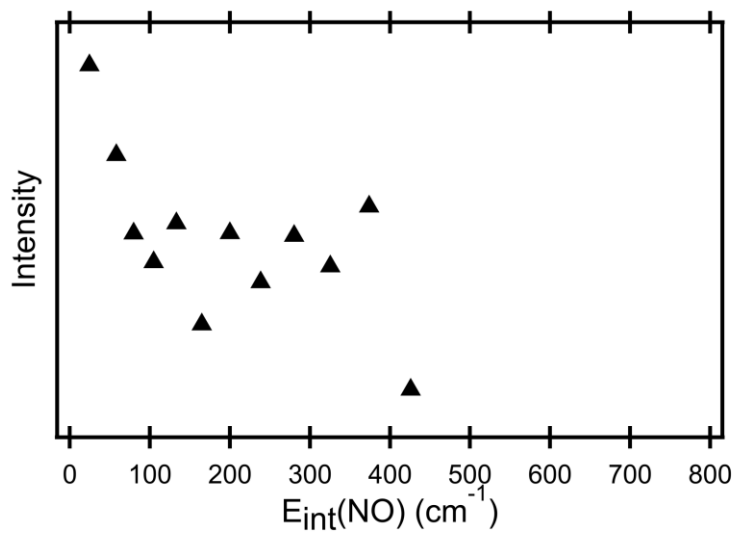


Figure 4.9. Product state distributions of NO ($X^2\Pi$, $v''=0$, $Q_1(J'')$) products from IR activation of NO-CH₄ complexes. IR activation energy of 3045 cm⁻¹.

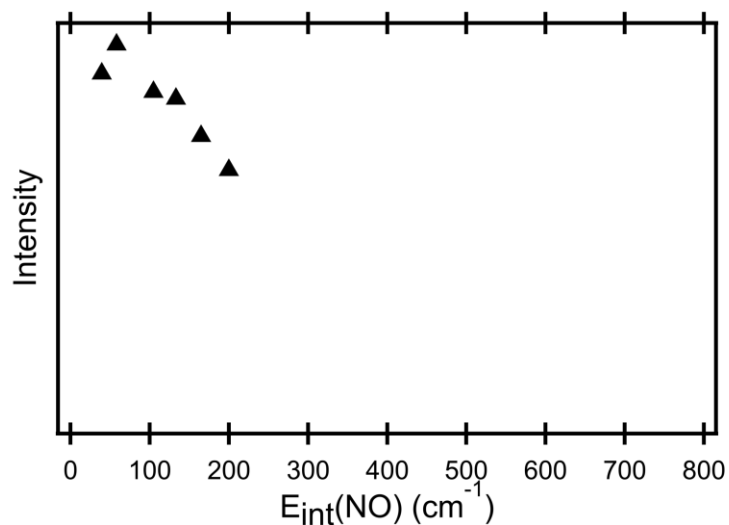


Figure 4.10. Product state distributions of NO ($X^2\Pi$, $v''=0$, $Q_2(J'')$) products from IR activation of NO-CH₄ complexes. IR activation energy of 3045 cm⁻¹.

The product state distributions were attempted to be fitted to a Boltzmann distribution to extract rotational temperature values. However, the corresponding Boltzmann distributions had R^2 values ranging from 0.3-0.7, which rendered these rotational temperatures inaccurate. Additionally, these product state distributions indicate a nonstatistical distribution across R(J'') and Q(J'') branches of NO products. Therefore, in the vicinity of the IR activated of the asymmetric CH stretch in the NO-CH₄ complex, there is a much more significant degree of nonstatistical behavior in the corresponding products, perhaps owing to the fast predissociation of NO-CH₄ as observed in select ion images.

4.4 Discussion

4.4.1 Vibrational Predissociation Dynamics.

In addition to generating an IR spectrum of NO-CH₄, the IR pump-UV probe method provides an approach to obtain insights into the Jahn-Teller dynamics

evolving on the ground NO-CH₄ vibrational state potential surface. Furthermore, the pair-correlated outcomes following vibrational predissociation of NO-CH₄ are revealed using IR activation of the asymmetric CH stretch with velocity map imaging (VMI) detection of NO ($X^2\Pi$, $v''=0$, J'' , F_n , Λ) products. The ion images and total kinetic energy release (TKER) distributions are shown in Figures 4.3-4.6. As observed in the figures, the degree of anisotropy in the ion images sensitively depends on the probed NO ($X^2\Pi$, $v''=0$, J'' , F_n , Λ) level, particularly as J'' changes. Following image reconstruction, the anisotropy parameter β for the slow and fast translational components in the TKER distributions were found to be $\sim+0.83$ and ~ 0 , respectively.

Illustrated in Figure 4.11, the TKER distribution for NO ($R_1(J''=10.5)$) products was fitted using Gaussian functions (green and gold traces). When the slow and fast translational Gaussian components from the fit are summed together, the combined simulation (red trace) is in good agreement with the experimental TKER distribution (black trace). Therefore, we conclude that the TKER distributions are bimodal and are a combination of a slow translational feature at $\sim 225 \text{ cm}^{-1}$ with a narrow envelope that appears dominantly for all NO (J'') and a fast translational component at $\sim 1400 \text{ cm}^{-1}$ with significantly greater broadening that varies in relative intensity as NO (J'') changes. The anisotropic ion image component, corresponding to the slow translational energy feature, is derived from a fast dissociation mechanism. Whereas the isotropic ion image component, correlating to the fast translational energy feature, arises from a slow

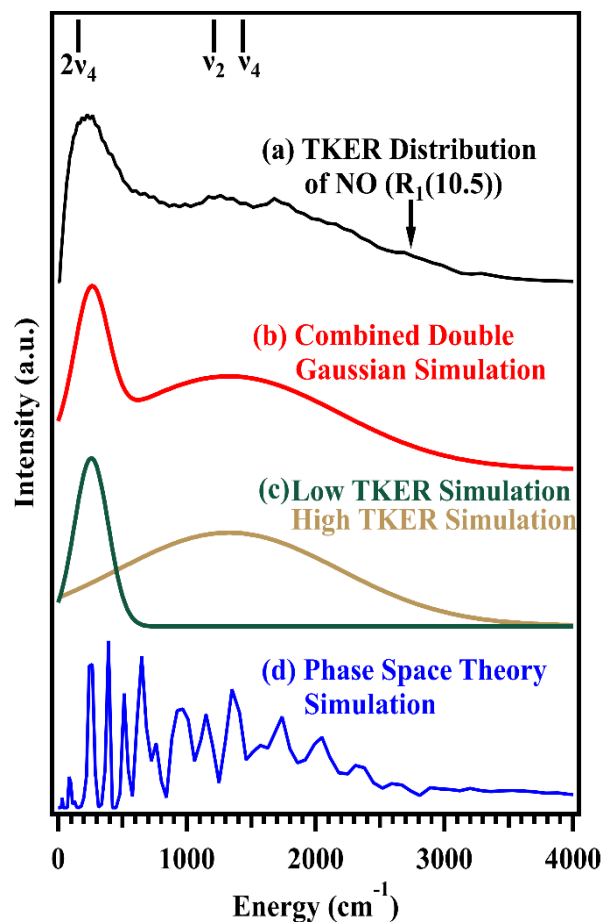


Figure 4.11: (a) Total kinetic energy release (TKER) of NO ($X^2\Pi$, $v''=0$, $R_1(J''=10.5)$) and CH_4 products from infrared activation of NO-CH_4 (black line). The accessible vibrational levels of CH_4 are provided relative to the available energy marked with an arrow. (b,c) Combined and individual Gaussian function fits, shown as red, green and gold lines, respectively, to the experimental data, revealing a bimodal translational distribution. (d) TKER distribution (blue line) from a phase space theory simulation is shown for comparison using CH_4 as the co-product.

fragmentation pathway. Since the slow translational energy feature is the dominant component in all TKER distributions, the fast dissociation mechanism appears to be the main pathway. This is consistent with the short vibrational predissociation lifetime of NO-CH₄ that contributes to the IR spectral broadening.

The experimental results in Figure 4.11 indicate that a sub-population of NO + CH₄ co-products are generated from a long-lived NO-CH₄ fragmentation pathway. Therefore, this slow dissociation mechanism, which occurs on a timescale greater than the NO-CH₄ rotational period (2.5 ps), points to NO-CH₄ fragmenting after statistically sampling the available degrees of freedom. Therefore, statistical Phase Space Theory (PST) simulations were carried out to predict the energy partitioning to relative translational energy between the NO ($X^2\Pi$, $v' = 0$, J'') + CH₄ co-fragments for comparison with the experimental TKER distributions. The PST simulation results are shown in the bottom blue trace of Figure 4.11.

PST provides a statistical treatment of energy partitioning with no dynamical constraints by requiring that all product quantum states have equal probability to be populated.¹⁷ Furthermore, the total angular momentum is conserved when employing PST, where the total angular momentum \mathbf{J} is the vector sum of the fragment angular momenta and the orbital angular momentum of the recoiling fragments \mathbf{L} , $\mathbf{J} = \mathbf{J}_{\text{NO}} + \mathbf{J}_{\text{CH}_4} + \mathbf{L}$. The simulated distributions are independent of the product interaction potential, thus making it applicable to infinitely attractive interaction potentials. The extent of the phase space available to each product channel is the radial flux along the reaction coordinate, which is the product of

the density of states for that channel and the relative radial velocity of the dissociation fragments. The PST distribution is straightforward to implement, yet it has several limitations such as not accounting for centrifugal barriers associated with the orbital angular momentum of products, which can be included as a constraint.⁶ Nevertheless, this method is employed to reveal the statistical energy distribution to translational energy and internal energy of the NO and CH₄ co-products. Overall, the agreement in Figure 4.11 between the experimental results and the predictions from PST theory are excellent. Therefore, the results indicate that the available degrees of freedom of NO-CH₄ have been sufficiently sampled for the slow dissociation pathway following vibrational predissociation of the complex.

4.4.2 Assignment of CH₄ vibrational modes

Previous studies^{7,18} have determined the intermolecular bond dissociation energy (D_0) of the NO-CH₄ complex to be $D_0 \sim 100 \text{ cm}^{-1}$. Using the following equation,

$$E_{avl} = E_{hv} - D_0 = TKER + E_{int}(NO) + E_{int}(CH_4)$$

along with the IR photon energy $E_{hv} = 3045 \text{ cm}^{-1}$ and D_0 from the literature, the available energy E_{avl} is distributed to relative translation (TKER) and the internal energy of the co-products, $E_{int}(NO)$ and $E_{int}(CH_4)$. With $E_{int}(NO)$ fixed when detecting NO ($R_1(J''=10.5)$), the E_{avl} is indicated with a black arrow superimposed on the experimental results in Figure 4.11. The TKER distribution intensity extends beyond E_{avl} , indicating that although the NO-CH₄ complexes are jet-cooled, they still possess a non-negligible degree of rotational energy. By

conservation of energy, when E_{avl} is placed into maximizing relative translation indicated by the black arrow in the figure, then $E_{int}(\text{CH}_4)$ is negligible. As translation decreases, the $E_{int}(\text{CH}_4)$ increases with the accessible vibrational modes¹⁹ of CH_4 shown as solid lines at the top of Figure 4.11. The ν_2 vibrational mode is predominantly a $-\text{CH}_2$ scissoring motion, whereas ν_4 is characterized as a $-\text{CH}_3$ umbrella mode of CH_4 . Indeed, the slow translational component overlaps well with two quanta placed in ν_4 and the fast translational feature coincides with either the ν_4 or ν_2 vibrational mode of CH_4 .

As observed in Figure 4.2, the Jahn-Teller distorted geometry of NO-CH_4 adopts a facial $-\text{CH}_3-\text{NO}$ configuration with NO perpendicular to the intermolecular axis. Prompt dissociation from this C_s configuration of NO-CH_4 leads to distortion largely along the umbrella motion of CH_4 . Therefore, we assign the slow translational feature at $\sim 225 \text{ cm}^{-1}$ in Figure 4.11 to activation of two quanta in the CH_4 (ν_4) mode. Additionally, there is little angular momentum imparted to the $\text{NO} + \text{CH}_4$ co-fragments resulting from this fast dissociation mechanism, consistent with the feature's narrow rotational envelope. In contrast, the fast translational component at $\sim 1400 \text{ cm}^{-1}$ in the TKER distribution has a much wider full-width at half maximum, and the angular distribution is isotropic signifying a slow dissociation mechanism. Here, CH_4 or NO may rotate around each other after IR activation of the NO-CH_4 complex, distributing energy into the ν_4 and ν_2 modes of CH_4 prior to complete fragmentation. Upon dissociating, significantly greater torque will be imparted to the products, therefore, increasing the breadth of this feature in the TKER distribution.

4.4.3 Jahn-Teller Mechanistic Pathways.

Figure 4.12 illustrates a qualitative overview of the dynamics before and after IR activation of the NO-CH₄ complex to NO ($X^2\Pi$, $v''=0$, J'' , F_n , Λ) + CH₄ products. As discussed in the previous section, the vibrational predissociation dynamics following IR excitation led to population of specific NO and CH₄ rovibrational states. However, to fully understand the product outcomes, one needs to account for the Jahn-Teller dynamics occurring prior to IR activation of the NO-CH₄ complex.

4.4.3.1 Dynamics Prior to IR Activation

As shown in Figure 4.12, NO-CH₄ adopts a lower-energy C_s configuration from the higher symmetry C_{3v} geometry, in which the N- or O-atom of NO directly points to the -CH₃ face of methane. The Jahn-Teller potential energy surfaces were adapted from Crespo-Otero.⁷ The doubly degenerate (E) symmetry of the C_{3v} geometry is broken into either the A'' or A' state with C_s symmetry when NO or CH₄ rotates. In this case, the C_{3v} geometry forms a conical intersection between the two A'' and A' electronic states. When the π^* molecular orbital of NO coincides with the plane of symmetry bisecting the -CH₃ face of methane, this leads to the higher energy A' state of NO-CH₄, whereas the lower energy A'' state is characterized by the NO π^* molecular orbital lying perpendicular to the plane of symmetry. Crespo-Otero⁷ calculated the energy gap between the A'' and A' states to be ~ 30 cm⁻¹. Additionally, they predicted the barriers from the A'' state to the C_{3v} configuration to be 78 cm⁻¹ and 53 cm⁻¹ for the A' state.

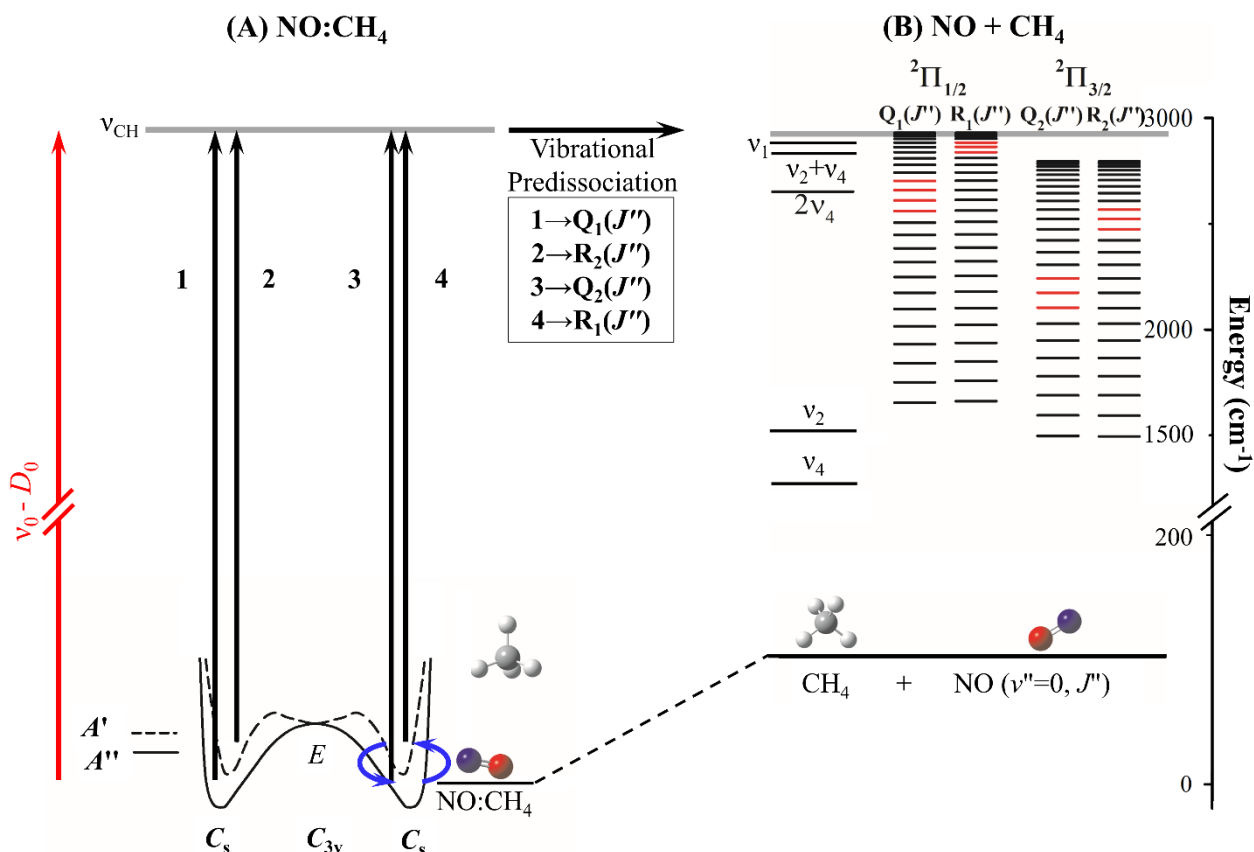


Figure 4.12: Energy level diagram illustrating the nonreactive bimolecular collision dynamics of NO-CH₄ complexes. (a) Jahn-Teller potential energy surfaces and dynamics of NO-CH₄ prior to IR activation. (b) NO-CH₄ complexes are prepared with one quantum in the asymmetric CH stretch (ν_{CH}) mode, leading to vibrational predissociation to NO ($X^2\Pi$, $\nu''=0$, J'' , F_n , Λ) + CH₄ co-products. The blue arrows signify that with sufficient zero-point and/or rotational energy, the NO-CH₄ complexes may interconvert between the A' and A'' electronic states within the C_s geometry or through the C_{3v} geometry. The red arrow on the left-hand side indicates the available energy to the products following IR excitation, $\nu_0 - D_0$, with the zero of energy defined as the NO ($X^2\Pi$, $\nu''=0$, Q₁(0.5)) + CH₄ asymptote. The black arrows show IR excitation of NO-CH₄ sub-populations, leading to vibrational predissociation and formation of symmetry-restricted NO ($X^2\Pi$, $\nu''=0$, J'' , F_n , Λ) + CH₄ co-products. The energetically allowed vibrational states of CH₄ fragments are shown correlating with NO ($\nu''=0$). On the right-hand side, the allowed spin-orbit ($^2\Pi_{1/2}$, $^2\Pi_{3/2}$) and rotational levels (J'') of NO ($\nu''=0$) products are shown following vibrational predissociation of NO-CH₄ (ν_{CH}). The red NO ($X^2\Pi$, $\nu''=0$, J'' , F_n , Λ) product levels indicate the ion images primarily displaying anisotropic angular distributions.

Crespo-Otero and co-workers⁷ determined that the NO-CH₄ complex is a dynamic Jahn-Teller system and may easily transition between the A' and A''

surfaces since their respective zero-point energies are near the barriers between the C_s and C_{3v} configurations. Furthermore, the ion images and TKER distributions indicate a non-negligible amount of rotational energy within the NO-CH₄ complex. The blue arrows in Figure 4.12 indicate the plausibility that the zero-point or rotational energy of NO-CH₄ may interconvert population between the A' and A'' electronic states through the C_{3v} geometry or within the C_s geometry, respectively. Population transfer from A' to A'' (and vice versa) through the C_{3v} configuration requires that either NO or CH₄ undergo rotation through this more highly symmetric geometry. The calculated harmonic frequencies for large amplitude motions of NO-CH₄ facilitating this nuclear rotation are 35 and 45 cm⁻¹; both motions have a' symmetry. Furthermore, rotation along the NO bond in the C_s configuration of NO-CH₄ will facilitate $A' \leftrightarrow A''$ electronic state interconversion. The methyl rotor mode (a'') of CH₄ calculated to be 16 cm⁻¹ mediates the intramolecular bond rotation of NO and therefore its π^* molecular orbital orientation with respect to the face of CH₄. Although the harmonic approximation is generally poor for such anharmonic nuclear motions, the calculated frequencies do provide an upper limit to the spacing between the rotor energy levels. Therefore, the ensemble of NO-CH₄ complexes will likely have distinct populations having either undergone $A' \leftrightarrow A''$ interconversion or not prior to IR excitation.

4.4.3.2 IR Activation Dynamics

In the absence of an external force, there are three degenerate asymmetric CH stretches of CH₄. Upon forming the NO-CH₄ complex, the slight perturbation

due to the NO intermolecular interaction with CH₄ breaks this triple degeneracy to form three distinct asymmetric CH stretches calculated to be separated by less than 3 cm⁻¹. Thus, two asymmetric CH stretches of NO-CH₄ become A'' symmetry in the C_s point group, while the third is totally symmetric A'. The asymmetric CH stretch with A' symmetry is characterized by a stretching of the facial -CH₃ bonds and a concomitant compression of the HC- bond. Using the ground state intermolecular bond dissociation energy ($D_0 \sim 100 \text{ cm}^{-1}$) determined previously^{7,18} and the asymmetric CH stretch frequency (ν_{CH}) of NO-CH₄ from the IR experiments presented here (3045 cm⁻¹), the available energy can be determined, $E_{\text{avl}} = 2945 \text{ cm}^{-1}$. Shown as the red arrow in Figure 4.12, E_{avl} (or $\nu_0 - D_0$) is partitioned to the translational and internal energies of the NO + CH₄ products. According to the well-known energy and momentum gap laws^{14,15}, E_{avl} will be distributed to minimize relative translation between recoiling products while maximizing energy placed into the spin-orbit, rotational, and vibrational degrees of freedom in NO ($X^2\Pi$, $\nu''=0$, J'' , F_n , Λ) + CH₄ fragments. Below E_{avl} , there are several vibrational states of CH₄ that may be accessed depending on the probed state of NO. The CH₄ vibrational modes are the two bending fundamentals (ν_4 and ν_2) at 1311 and 1533 cm⁻¹, a bending overtone level $2\nu_4$ at 2587 cm⁻¹, the $\nu_2+\nu_4$ combination band at 2830 cm⁻¹, and the totally symmetric CH stretch ν_1 at 2917 cm⁻¹.¹⁹ Energy transfer to the two bending fundamentals is not expected to contribute significantly to the prompt predissociation mechanism since these levels lie far from resonance (large energy gap). In contrast, energy transfer to the $2\nu_4$, $\nu_2+\nu_4$, and ν_1 levels will minimize translational energy release

and will provide the major pathway for predissociation of NO-CH₄ (ν_{CH}) via an intramolecular vibration-to-vibration energy transfer process within the CH₄ monomer. Due to the fact that NO-CH₄ adopts a C_s configuration with NO oriented perpendicular to the -CH₃ face, the likely CH₄ vibrational level to be populated is the 2 ν_4 state since it has the same umbrella motion as the A' asymmetric CH stretch mode of NO-CH₄ inducing prompt dissociation. In addition to energy conservation, the total symmetry must be conserved during the vibrational predissociation of NO-CH₄ to products.

4.4.3.3 Mechanistic Pathways

The ion images and TKER distributions show a bimodal distribution, in which the slow translational feature corresponds to a prompt dissociation pathway and the fast translational component correlates to a slow dissociation pathway. First focusing on the prompt dissociation pathway, Figure 4.12 shows four possible mechanisms (black arrows) by which NO-CH₄ complexes may evolve to fragments. Each mechanism is distinguished by whether a particular NO-CH₄ sub-population originated on the A'' or A' electronic state surface and whether the sub-population experienced A'' \leftrightarrow A' interconversion prior to IR activation. Here, we recorded the ion images for the different spin-orbit (F_1 and F_2) and Λ -doublet ($\Pi(A'')$ and $\Pi(A')$) levels using the Q₁(J''), R₁(J''), Q₂(J''), and R₂(J'') lines of NO products. In particular, the Q-branch transitions have a high selectivity for the $\Pi(A'')$ state, whereas the $\Pi(A')$ state may be probed with the R-branch (or P-branch) transitions.²⁰

Considering mechanism 1 with NO-CH₄ complexes originating on the lower A'' surface and not having undergone A'' ↔ A' interconversion, excitation of the fundamental asymmetric CH stretch involving $\nu_{\text{CH}}=1 \leftarrow \nu_{\text{CH}}=0$, each with a' symmetry results in a parallel vibrational transition. This is consistent with the parallel anisotropic angular distribution ($\beta \sim +0.83$) belonging to the anisotropic feature in the ion images and the corresponding slow translational component in the TKER distributions. The C_s point group is isomorphic with the T_d point group of higher symmetry, and we make this transformation here to use a common point group between the reactants and products to confirm that symmetry is conserved. Therefore, A' and A'' belonging to C_s transform to A₁ and A₂, respectively, within the T_d point group. Considering the symmetry of the transition for mechanism 1 along with the three possible nuclear spin isomers with A, E, and F (or T) symmetry in the T_d point group of CH₄, the reactants total symmetry is

$$\Gamma_{\text{electronic}} \otimes [\Gamma_{\nu'} \otimes \Gamma_{\nu''}] \otimes \Gamma_{\text{nuclear spin}} = A_2 \otimes [a_1 \otimes a_1] \otimes [A_1, E, \text{or } T] = A_2 \oplus E \oplus T_1 \oplus T_2.$$

The NO-CH₄ complexes then undergo prompt vibrational predissociation to NO (X²Π, $\nu''=0$, J'', F_n, Λ) + CH₄ (2ν₄) products. Detecting NO products using the Q₁(J'') or Q₂(J'') spin-orbit transitions have the necessary A₂ symmetry to conserve the total symmetry between reactants and products. The total symmetry of the products is,

$$\Gamma_{\text{NO}} \otimes \Gamma_{\text{CH}_4}(2\nu_4) = A_2 \otimes [t_2 \otimes t_2] = A_2 \oplus E \oplus T_1 \oplus T_2.$$

We tentatively assign mechanism 1 to the formation of NO $Q_1(J'')$ products that report on the vibrational predissociation of NO-CH₄ originating on the lower A_2 surface. Using a similar symmetry argument, we tentatively assign mechanism 2 to the direct dissociation of NO-CH₄ on the higher-energy A_1 surface and formation of NO $R_2(J'')$ products. Similar to mechanism 1, the NO-CH₄ complex in mechanism 2 also undergoes rapid dissociation near resonant to the CH₄ ($2\nu_4$) state due to effective energy transfer. Furthermore, there is a slight difference in the populated rotational levels (labeled as red lines on the right-hand side of Figure 4.12) of the NO($Q_1(J'')$) and NO($R_2(J'')$) spin-orbit states derived from prompt NO-CH₄ vibrational predissociation. In particular, NO($Q_1(J'')$) occupies somewhat lower rotational levels compared to NO($R_2(J'')$), which is consistent with the energy difference between the A_1 and A_2 surfaces of NO-CH₄. As we will show, the formation of NO fragments in the $R_1(J'')$ and $Q_2(J'')$ spin-orbit states likely arise from alternative pathways.

A similar symmetry argument employed for mechanisms 1 and 2 can be extended to mechanisms 3 and 4 to account for NO($Q_2(J'')$) and NO($R_1(J'')$) product formation. Again, the total symmetry of reactants must be conserved in the resulting products following NO-CH₄ vibrational predissociation. Illustrated in the spin-orbit distributions in Figure 4.12, there is a much greater polarization in the populated rotational states of NO($Q_2(J'')$) and NO($R_1(J'')$) highlighted as red lines, where the ion images indicated prompt dissociation from the anisotropic angular distributions. Indeed, lower rotational states of NO($R_1(J'')$) products are preferred, whereas there is a propensity to occupy larger rotational states for

NO(Q₂(J'')). To account for the loss or gain in angular momentum, A₁ ↔ A₂ population transfer of the NO-CH₄ reactant complexes is considered.

We tentatively assign the formation of NO(Q₂(J'')) products arising from mechanism 3, whereby NO-CH₄ population initially on the higher-energy A₁ state transfers to the lower A₂ surface. As discussed previously, this may arise either from the zero-point and/or rotational energy of the NO-CH₄ complexes enabling A₁ → A₂ interconversion, plausibly through specific large-amplitude motions sampling different Jahn-Teller geometries. Following mechanism 3, the NO-CH₄ complexes now on the A₂ surface become vibrationally activated and thus predissociate to NO(Q₂(J'')) + CH₄ products. Here, the overall symmetry constraints are met as discussed for mechanism 1. Additionally, the increase in angular momentum from A₁ → A₂ interconversion is imprinted on the NO(Q₂(J'')) products with large rotational states occupied following prompt NO-CH₄ dissociation. In similar fashion, mechanism 4 is differentiated by a subset of NO-CH₄ complexes undergoing A₂ → A₁ population transfer, and in doing so, lose angular momentum shown as a propensity for NO(R₁(J'')) products to occupy low rotational states. Total symmetry conservation from reactants to products is also maintained. The slow translational component in both NO(Q₂(J'')) and NO(R₁(J'')) TKER distributions may be assigned to CH₄ (2ν₄), in agreement with NO(Q₁(J'')) and NO(R₂(J'')). However, the slow translational feature in the TKER distributions of NO(Q₂(J'')) and NO(R₁(J'')) may also be assigned to either the ν_{2+ν₄} or ν₂ modes of CH₄ due to their energetic proximity to the populated spin-orbit levels.

The prompt vibrational predissociation of NO-CH₄ is the primary pathway leading to NO + CH₄ products, conceivably arising from the four mechanisms discussed above. However, the TKER distributions indicate that as the probed rotational state of NO ($X^2\Pi$, $v''=0$, J'' , F_n , Λ) changes, a fast translational feature peaking at $\sim 1400\text{ cm}^{-1}$ with a broad *fwhm* increasingly gains intensity. As Figure 4.11 shows, the fast translational component overlaps well with a single quantum placed in either the v_4 or v_2 vibrational mode of CH₄ fragments. Furthermore, the anisotropy parameter β is approximately zero across this translational feature, revealing an isotropic angular distribution and thus a slow dissociation mechanism at play. Following IR activation of NO-CH₄ to $v_{\text{CH}}=1$, a population subset may sample geometries other than that required for prompt dissociation, leading to a longer vibrational dissociation lifetime than the rotational period of NO-CH₄ ($\tau < 2.5\text{ ps}$). As either NO or CH₄ monomers rotate following vibrational excitation, the energy initially deposited into the asymmetric CH stretch of NO-CH₄ may be statistically distributed into other available rovibrational states of NO and CH₄ co-fragments. In addition to the v_4 mode of CH₄ accepting energy due to deformation of the facial -CH₃ atoms, other nuclear displacements such as the -CH₂ scissoring mode (v_2) may be induced from NO interacting with additional sites of the CH₄ monomer. Moreover, the additional torque within the long-lived NO-CH₄ complexes will be imprinted on the NO + CH₄ products, consistent with the rotationally broadened translational feature at 1400 cm^{-1} in the TKER distributions.

This physical picture of the slow dissociation mechanism for NO-CH₄ complexes sampling a greater number of monomer orientations is in agreement with previous inelastic scattering experiments of NO with CH₄ from Wang and coworkers.²¹ The authors revealed differing degrees of CH₄ product rotational excitation depending on the collision conditions. For glancing NO + CH₄ collisions with a large impact parameter, the collision reactants may have a large degree of orientations upon bimolecular collision. Wang et al showed that these collisions resulted in a large torque or rotational excitation of CH₄ products due to the carbon atom bearing the center-of-mass. Their results are qualitatively consistent with the results presented here.

We now turn to a possible explanation for the peculiar dynamics of NO-CH₄, which is the plausibility that nonadiabatic transitions may be occurring on the Jahn-Teller surfaces prior to IR activation resulting in a geometric phase impacting the dynamical outcomes. As discussed previously, Crespo-Otero⁷ determined the zero-point energy of NO-CH₄ to be near the barriers between the C_s and C_{3v} configurations, therefore classifying this complex as a dynamic Jahn-Teller system. Furthermore, there is a nonnegligible degree of NO-CH₄ rotational excitation indicated from the experimental results. Crespo-Otero⁷ calculated the energy gap between the A'' and A' states to be ~30 cm⁻¹. Additionally, they predicted the barriers from the A'' state to the C_{3v} configuration to be 78 cm⁻¹ and 53 cm⁻¹ for the A' state, and the authors showed that the C_{3v} geometry forms a conical intersection between the two A'' and A' electronic states. Therefore, the zero-point or rotational energy of NO-CH₄ may interconvert population between

the A' and A'' electronic states through the C_{3v} geometry or within the C_s geometry. The changing orientation of the NO π^* molecular orbital with respect to the face of CH₄ also changes the NO-CH₄ electronic state symmetry. Large-amplitude motions mediating this $A' \leftrightarrow A''$ nonadiabatic transition include hindered rotor modes that are conceivably populated prior to IR activation.

As shown with the experimental results, IR-induced dissociation of NO-CH₄ leading to NO ($X^2\Pi$, $v''=0$, J'' , F_n , Λ) + CH₄ products reveals dramatic changes to the ion image anisotropy and corresponding TKER distributions with striking J'' -level dependence. As qualitatively shown in the energy-level diagram in Figure 4.11, we hypothesize that as the dynamic Jahn-Teller NO-CH₄ system encircles the conical intersection formed between two states with C_{3v} or C_s geometries, the dynamical mechanisms are imprinted on the symmetry-restricted products. Since we observe such polarized results encoded in the spin-orbit states of NO products, future work will include performing dynamics simulations on high-level surfaces to report on a possible geometric phase changing the electronic wavefunction sign of NO-CH₄ as the system samples the C_{3v} and C_s geometries. Geometric phases have primarily been reported from theory predictions^{22–24} to drastically impact the nonadiabatic dynamics. Previous theoretical work by Subotnik²³ has shown that for a radical reaction with two outgoing channels, nuclear motion and the presence of a geometric phase can induce spin selectivity in the products as large as 100%. Nonadiabatic effects imprinted as polarizing populations in the spin-orbit distributions of NO ($X^2\Pi$, $v''=0$, J'' , F_n , Λ) will test these hypotheses. Testing this hypothesis will require precise dynamics

simulations with (diabatic) and without (adiabatic) a geometric phase as NO-CH₄ encircles the conical intersection to NO product symmetry states.

4.5 Conclusions

We have reported an in-depth study, on the molecular level, of the nonreactive collision dynamics of NO with CH₄ by utilizing infrared activation of NO-CH₄ in combination with velocity map imaging of NO ($X^2\Pi$, $v''=0$, J'' , F_n , Λ). The ion-images' angular distribution (or anisotropy) depend sensitively on the probed rotational quantum number of NO (J'') products. We conclude that there are two subsets of NO fragments which are defined by their dissociative timescale. A subset in which the ion images and TKER distributions show an anisotropic component at low relative translation indicating prompt dissociation due to effective vibration-vibration energy transfer; and, a smaller subset which is defined by an isotropic feature at high relative translation signifying a slow dissociative timescale due to increased sampling of each co-product's respective energy space.

In addition to predissociation dynamics of NO-CH₄ following vibrational excitation, the Jahn-Teller dynamics prior to infrared activation must be considered to fully describe the product spin-orbit distributions. Thus, we hypothesize that the product spin-orbit distributions depend sensitively on the originating ground-state NO:CH₄ electronic state, A' or A'' .

Lastly, we conclude that activation of the asymmetric CH stretch of CH₄ will have substantial effects on the decay rates and energy exchange rates between NO and CH₄ in the atmosphere and in combustion environments.

Compared to NO and CH₄ reactant collisions with translational or rotational excitation, our results indicate that the nonreactive collision rate between NO and CH₄ will be greatly accelerated when CH₄ becomes vibrationally activated along the asymmetric CH stretch prior to collision. The energy exchange rate and the internal energies of the products will also be impacted as shown by the experimental results.

4.6 References

- (1) Bersuker, I. *The Jahn-Teller Effect*; Cambridge University Press: University Press, Cambridge, 2006.
- (2) Bersuker, I. B. *The Jahn-Teller Effect and Vibronic Interactions in Modern Chemistry*; Modern Inorganic Chemistry; Plenum Press, New York and London: New York, 1984.
- (3) Beswick, J. A.; Jortner, J. Intramolecular Dynamics of Van Der Waals Molecules. In *Advances in Chemical Physics*; John Wiley & Sons, Ltd, 1981; pp 363–506. <https://doi.org/10.1002/9780470142677.ch7>.
- (4) Ewing, G. E. Selection Rules for Vibrational Energy Transfer: Vibrational Predissociation of van Der Waals Molecules. *J. Phys. Chem.* **1987**, *91* (18), 4662–4671. <https://doi.org/10.1021/j100302a008>.
- (5) von Busch, H.; Dev, V.; Eckel, H.-A.; Kasahara, S.; Wang, J.; Demtröder, W.; Sebald, P.; Meyer, W. Unambiguous Proof for Berry's Phase in the Sodium Trimer: Analysis of the Transition $A^2 E'' \leftarrow X^2 E'$. *Phys. Rev. Lett.* **1998**, *81* (21), 4584–4587. <https://doi.org/10.1103/PhysRevLett.81.4584>.
- (6) Baer, T.; Hase, W. L. *Unimolecular Reaction Dynamics: Theory and Experiments*; Oxford University Press, 1996.
- (7) Crespo-Otero, R.; Suardiaz, R.; Montero, L. A.; García de la Vega, J. M. Potential Energy Surfaces and Jahn-Teller Effect on CH₄···NO Complexes. *J. Chem. Phys.* **2007**, *127* (10), 104305. <https://doi.org/10.1063/1.2752805>.
- (8) Wheeler, M. D.; Tsiouris, M.; Lester, M. I.; Lendvay, G. OH Vibrational Activation and Decay Dynamics of CH₄–OH Entrance Channel Complexes. *J. Chem. Phys.* **2000**, *112* (15), 6590–6602. <https://doi.org/10.1063/1.481232>.
- (9) Tsiouris, M.; Wheeler, M. D.; Lester, M. I. Activation of the CH Stretching Vibrations in CH₄–OH Entrance Channel Complexes: Spectroscopy and Dynamics. *J. Chem. Phys.* **2001**, *114* (1), 187–197. <https://doi.org/10.1063/1.1328747>.
- (10) Tsiouris, M.; Pollack, I. B.; Lester, M. I. Infrared Action Spectroscopy and Inelastic Recoil Dynamics of the CH₄–OD Reactant Complex. *J. Phys. Chem. A* **2002**, *106* (34), 7722–7727. <https://doi.org/10.1021/jp0209143>.
- (11) Wen, B.; Meyer, H. The near IR Spectrum of the NO($\chi^2 \Pi_2$)–CH₄ Complex. *J. Chem. Phys.* **2009**, *131* (3), 034304. <https://doi.org/10.1063/1.3175556>.
- (12) Blackshaw, K. J.; Quartey, N.-K.; Korb, R. T.; Hood, D. J.; Hettwer, C. D.; Kidwell, N. M. Imaging the Nonreactive Collisional Quenching Dynamics of NO ($A^2 \Sigma^+$) Radicals with O₂ ($X^3 \Sigma_g^-$). *J. Chem. Phys.* **2019**, *151* (10), 104304. <https://doi.org/10.1063/1.5109112>.
- (13) Blackshaw, K. J.; Ortega, B. I.; Quartey, N.-K.; Fritzeen, W. E.; Korb, R. T.; Ajmani, A. K.; Montgomery, L.; Marracci, M.; Vanegas, G. G.; Galvan, J.; Sarvas, Z.; Petit, A. S.; Kidwell, N. M. Nonstatistical Dissociation Dynamics of Nitroaromatic Chromophores. *J. Phys. Chem. A* **2019**, *123* (19), 4262–4273. <https://doi.org/10.1021/acs.jpca.9b02312>.

- (14) Pan, C.; Zhang, Y.; Lee, J. D.; Kidwell, N. M. Imaging the Dynamics of CH₂ BrI Photodissociation in the Near Ultraviolet Region. *J. Phys. Chem. A* **2018**, *122* (15), 3728–3734. <https://doi.org/10.1021/acs.jpca.7b12268>.
- (15) Dribinski, V.; Ossadtchi, A.; Mandelshtam, V. A.; Reisler, H. Reconstruction of Abel-Transformable Images: The Gaussian Basis-Set Expansion Abel Transform Method. *Rev. Sci. Instrum.* **2002**, *73* (7), 2634–2642. <https://doi.org/10.1063/1.1482156>.
- (16) Luque, J.; Crosley, D. R. LIFBASE, 2013.
- (17) Levine, R. D. *Molecular Reaction Dynamics*; Cambridge University Press: Cambridge, 2009.
- (18) Tamé-Reyes, V. M.; Gardner, A. M.; Harris, J. P.; McDaniel, J.; Wright, T. G. Spectroscopy of the \tilde{A} State of NO–Alkane Complexes (Alkane = Methane, Ethane, Propane, and *n*-Butane). *J. Chem. Phys.* **2012**, *137* (21), 214307. <https://doi.org/10.1063/1.4768811>.
- (19) Wenger, Ch.; Champion, J. P. Spherical Top Data System (STDS) Software for the Simulation of Spherical Top Spectra. *J. Quant. Spectrosc. Radiat. Transf.* **1998**, *59* (3), 471–480. [https://doi.org/10.1016/S0022-4073\(97\)00106-4](https://doi.org/10.1016/S0022-4073(97)00106-4).
- (20) Andresen, P.; Rothe, E. W. Analysis of Chemical Dynamics via Λ Doubling: Directed Lobes in Product Molecules and Transition States. *J. Chem. Phys.* **1985**, *82* (8), 3634–3640. <https://doi.org/10.1063/1.448897>.
- (21) Wang, X.-D.; Robertson, P. A.; Cascarini, F. J. J.; Quinn, M. S.; McManus, J. W.; Orr-Ewing, A. J. Observation of Rainbows in the Rotationally Inelastic Scattering of NO with CH₄. *J. Phys. Chem. A* **2019**, *123* (36), 7758–7767. <https://doi.org/10.1021/acs.jpca.9b06806>.
- (22) Xie, C.; Yarkony, D. R.; Guo, H. Nonadiabatic Tunneling via Conical Intersections and the Role of the Geometric Phase. *Phys. Rev. A* **2017**, *95* (2), 022104. <https://doi.org/10.1103/PhysRevA.95.022104>.
- (23) Wu, Y.; Subotnik, J. E. Electronic Spin Separation Induced by Nuclear Motion near Conical Intersections. *Nat. Commun.* **2021**, *12* (1), 700. <https://doi.org/10.1038/s41467-020-20831-8>.
- (24) Xie, C.; Zhao, B.; Malbon, C. L.; Yarkony, D. R.; Xie, D.; Guo, H. Insights into the Mechanism of Nonadiabatic Photodissociation from Product Vibrational Distributions. The Remarkable Case of Phenol. *J. Phys. Chem. Lett.* **2020**, *11* (1), 191–198. <https://doi.org/10.1021/acs.jpcllett.9b03407>.

Chapter 5: Larger NO-alkane Van der Waals Complexes

5.1 Introduction

Chapters 3 and Chapter 4 present a rigorous study of the weakly bound complex between nitric oxide and methane (NO-CH₄). Firstly, we have reported the vibrational spectroscopy of the NO-CH₄ bimolecular collision complex. We recorded the resonant ion-depletion infrared spectra and infrared action spectra of NO-CH₄ in the CH₄ antisymmetric stretching region. Additionally, we have reported an in-depth, molecular-level study of the nonreactive collision dynamics of NO with CH₄ by investigating the NO-CH₄ complex along the bimolecular collision pathway. To this end, we utilized infrared activation in combination with velocity map imaging of NO ($X^2\Pi$, $v''=0$, J'' , F_n , Λ) products. We aim to leverage similar spectroscopic and dynamics techniques to understand the bimolecular collision pathways of larger hydrocarbon NO-alkanes (alkane=propane, ethane, *n*-butane).

The study of NO-alkanes is pertinent, as described previously, due to the presence of both species in combustion and atmospheric environments. In the troposphere, the emissions of NO and hydrocarbons (alkanes) lead to a complex series of chemical and physical transformations which result in drastic effects.¹ These range from the formation of ozone in urban and regional areas as well as in the global troposphere to acid decomposition and the formation of secondary particulate matter through gas/particle partitioning of both emitted chemical compounds and the atmospheric reaction products.¹ Therefore, the nature of the initial reaction between the NO and the alkane molecule would aid in

understanding the presence or absence of such reactivity.² Additionally, from a physical chemistry perspective, the interaction of NO, an open-shell molecule, with closed-shell alkanes is fundamentally interesting as their interactions fall between full chemical bonding and van der Waals interactions.² These short-lived complexes are formed along the bimolecular collision reaction coordinate, and the result of these interactions can affect the reactivity of the collision partners. The most pertinent systems of interest are NO complexed with the four lightest alkanes (methane, ethane, propane, *n*-butane). NO-CH₄ has previously received much attention³⁻⁷; however, there have only been a few studies on NO-ethane, NO-propane, and NO-(*n*-butane).

5.2 Previous Studies on Higher Order NO-alkanes

Wright et al. recorded the $A \leftarrow X$ transitions of NO-ethane (NO-C₂H₆) and NO-(ethane)₂ (NO-(C₂H₆)₂) using (1+1) resonance-enhanced multiphoton ionization spectroscopy in 2000.⁸ From the spectrum, they were able to extract the dissociation energies for both the *A* and *X* states. The dissociation energy, D_0' , of the *A* state was measured to be 340 cm⁻¹ and the dissociation energy D_0'' of the *X* state was determined to be 190 cm⁻¹.⁸ Additionally, they observed a vibronic progression of 40 cm⁻¹, which similarly to NO-CH₄, was assigned to the intermolecular stretch. The spectrum was found to be partially resolved, but difficult to make full assignments; however, using the NO/ethane mixture, they were able to record a spectrum in the NO-(C₂H₆)₂ channel. Although this weak spectrum was difficult to interpret, they were able to use it to confirm that a rise in the NO-C₂H₆ signal was associated with the dissociation of the NO-(C₂H₆)

complex.⁸ Finally, there were indications that the *A* state of NO-(C₂H₆)₂ is dissociative along the NO-(C₂H₆)...-(C₂H₆) coordinate.⁸

In 2012, Wright et al. revisited NO-CH₄ and NO-C₂H₆, and also reported the R2PI spectra for NO-(propane) and NO-(*n*-butane) for the first time.² The spectra for NO-CH₄ and NO-C₂H₆ were consistent with their previous work. For NO-C₂H₆, they concluded that the NO molecule is aligned parallel to a C-C bond of ethane.² In the case of the NO-C₂H₆, they were able to record a spectrum for NO-(C₂H₆)₂ and NO-(C₂H₆)₃. It was observed that the fragmentation of higher order clusters were contributing to the spectra in the lower mass channels.² Therefore, they did not attempt to record spectra in the NO mass channel since

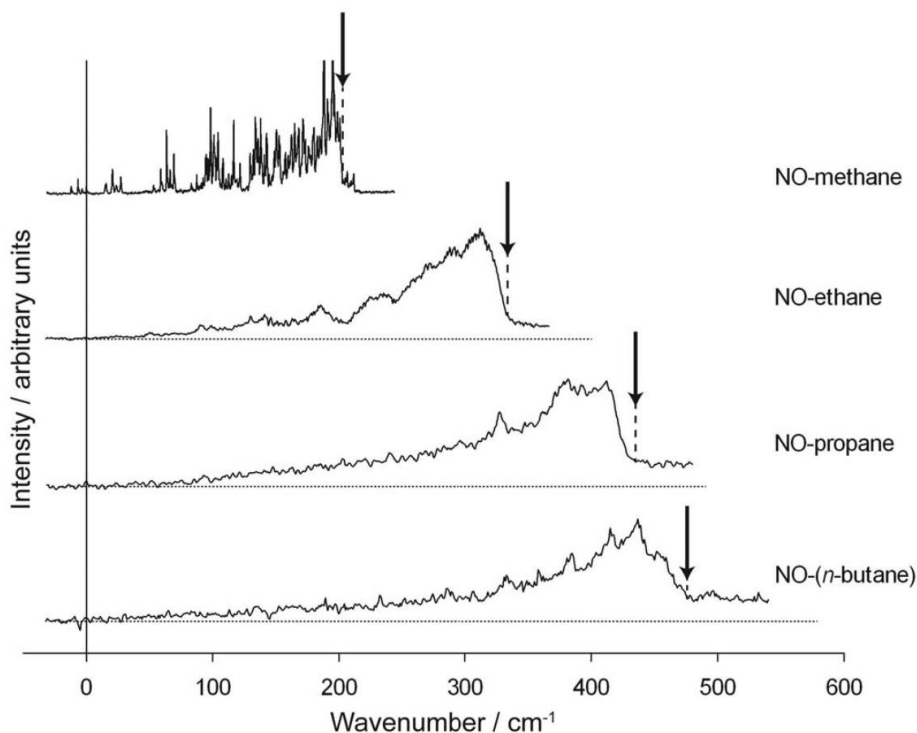


Figure 5.1. (1+1) REMPI spectra of NO-alkane spectra, showing the region associated with the 1:1 complexes. The arrows mark the positions of the band onsets and offsets.¹

there was NO^+ signal intensity that was arising from significant non-resonant ionization.

From comparison across the NO-alkane UV spectra shown in Figure 5.1, there was a monotonic increase in the experimental dissociation energy as the alkane chain increased, which is in line with the increasing polarizability values.² Additionally, the interaction energy of the NO with the respective alkane is also strongly dependent on the intermolecular separation; repulsion terms, and higher-order attractive terms may also play a key role.^{2,8} Experimental D_0' values indicated that the binding in the *A* state is stronger than that of the *X* state.² This can be explained by a consistent red-shift across all 1:1 NO-alkane complexes with respect to the uncomplexed NO origin. Additionally, there was confirmed fragmentation of higher order complexes contributing to all 1:1 NO-alkane UV spectra at higher energy, which was past the initial drop off of the parent complex. Finally, the observations of higher-order complexes suggest that in the $\text{NO}-(\text{alkane})_n$ complexes ($n > 1$), the alkane molecules could be reacting with one another.²

Thus, it is obvious that the increase in alkane chain length is leading to unresolved interactions in NO-alkane complexes. The structure of the complexes is largely in question and how the increase in chain length affects the individual reactivity of NO and alkanes is not well understood. Therefore, our goal will be to better understand the bimolecular collision dynamics of higher order NO-alkane complexes.

5.3 Proposed Studies

5.3.1 NO-Ethane

The initial studies of NO-C₂H₆ suggest that the weakly bound molecular complex has complicated interactions, which make the experimental UV spectroscopy data difficult to disentangle. In contrast to the UV spectra of NO-CH₄, the NO-C₂H₆ UV spectra lack any concrete structure, which renders the UV spectrum difficult to disentangle. A possible explanation for this is that there are more contributions, likely from low-lying intramolecular modes of the alkanes and lower frequency intermolecular modes.^{2,8} Additionally, the low-lying minima, similar to NO-CH₄, suggest large amplitude motion of the NO-C₂H₆ complex.^{2,3} The comparison of data between NO-CH₄ and NO-C₂H₆ therefore would aid in understanding how alkane size effects the interactions and subsequent dynamics of these collision complexes. NO-C₂H₆ is hypothesized to not experience the Jahn-Teller effect because it lacks a geometry whereby the electronic state of the complex can be described as a degenerate state.^{2,3,8} This is in direct contrast to NO-CH₄, where the potential energy surfaces correspond to the splitting of the ²Π electronic degeneracy of the NO molecule.

Therefore, additional studies are needed to help understand the different contributions to the geometry that the NO-C₂H₆ complex adapts throughout the dissociation coordinate. Therefore, we propose to characterize these subtle inter- and intramolecular interactions by utilizing IR spectroscopy in the fundamental CH₄ stretching region. Similarly, to NO-CH₄, the R2PI of NO-C₂H₆ will inform consequent resonant excitation of the complex. Thus, we aim to leverage resonant ion-depletion infrared spectroscopy of the fundamental CH₄ stretching

region and the overtone CH₄ stretching region. Comparison of these infrared spectra with computational calculations and simulations will thereby aid in understanding the geometry the NO-C₂H₆ complex adopts along the collision coordinate. Finally, the homogeneous linewidths of these infrared spectra would aid in characterizing the lifetime of this short-lived complex.

By utilizing this background on the interactions of the complex, subsequent spectroscopy and dynamics studies would be carried out. In previous studies of NO-C₂H₆, it has been noted that there are contributions from both the 1:1 complex and from NO-(C₂H₆)_n (n>1) and these contributions are noted in the R2PI spectrum. Thus, it would be plausible to obtain conformationally specific infrared spectra of NO-C₂H₆ and NO-(C₂H₆)₂ using resonant ion-dip infrared spectroscopic. Furthermore, if the complexes had differing infrared absorption energies, these differences could be utilized for subsequent dynamics studies. By monitoring NO⁺, we would aim to scan the tunable infrared radiation and obtain infrared action spectra of products resulting from NO-C₂H₆ and NO-(C₂H₆)₂. This would only be plausible if we confirm the existence of higher order ethane clusters generated from our supersonic jet expansion. If NO-C₂H₆ is the sole cluster generated, then we would aim to monitor NO⁺, and scan the IR wavelength to obtain infrared action spectra of NO-C₂H₆. Finally, as described in Chapter 2, by changing the resonant UV probe wavelength and scanning the IR wavelength, infrared action spectra specific to varying NO ($X^2\Pi$, $v'=0$, J' , F_n , Λ) would be generated. This would aid in determining if there are differing mechanisms by which NO-C₂H₆ dissociates.

In addition to generating the infrared action spectrum of NO-C₂H₆, the IR pump-UV probe method provides an approach to obtain specific insights into the dynamics evolving on the ground NO-C₂H₆ vibrational state potential energy surface. By utilizing the infrared action spectrum, the infrared wavelengths that prompt dissociation of the complex would be identified, and subsequent velocity-map imaging studies would be performed to understand the energy-exchange mechanisms. The specific outcomes following dissociation of NO-C₂H₆ would be revealed using IR activation of the asymmetric CH stretch with velocity map imaging detection of NO ($X^2\Pi$, $v'=0$, J' , F_n , Λ) products. The corresponding ion images would reveal important information on the dissociative time scale of the complex. By integrating these ion images as previously described, total kinetic energy release (TKER) distributions can be obtained. The TKER distributions would reveal important insights into how and where energy flows following dissociation of the complex. These results can be compared and contrasted to that of NO-CH₄, which would aid in further characterizing and explaining how the Jahn-Teller effect manifests in such complexes. Finally, if the presence of NO-(C₂H₆)₂ is confirmed and its action spectrum is identified, it would be subject to similar dynamics studies.

NO-C₂H₆ offers the opportunity of exploring many important physical and chemical phenomena. The complex offers a unique opportunity to explore not only how chain length affects the structure of atmospheric species but also the dynamics and subsequent reactivity. Additionally, the comparison to NO-CH₄ would aid in further understanding how Jahn-Teller distortion affects polyatomic

gas-phase species. Finally, these results would aid in determining how the increase in hydrocarbons and nitric oxide is affecting important atmospheric processes. These results therefore of broad interest to the atmospheric and combustion chemistry communities, in addition to the physical chemistry community to test theoretical predictions of the bimolecular collision outcomes.

5.3.2 Higher Order NO-Alkanes

As the alkane chain length increases, it becomes more likely that NO-(alkane)_n (n>1) will be generated as well. Through analysis of the R2PI spectra previously recorded, it has been hypothesized that in the NO-(alkane)_n complexes (n>1), the alkane molecules are interacting with each other. Therefore, the proposed experiments on longer chain-length NO-alkanes are subject to the presence of these higher-order complexes. Wright et al². were not able to detect higher order clusters in the mass spectra owing to dissociation after electronic excitation/ionization.

Therefore, the proposed experiments would build upon those for NO-C₂H₆. We first propose to investigate NO-propane and NO-*n*-butane by resonant ion-depletion spectroscopy. Depending on the prevalence of higher order complexes, an array of dynamics studies would follow. These dynamics studies would be based on the infrared action spectra since this would relay information on the formation of products. Thereafter, subsequent velocity map imaging studies would commence to understand the energy flow following dissociation of 1:1 NO-alkane complexes as well as possible NO-(alkane)_n (n>1). These results would

aid in characterizing the affect chain length has on the chemical properties and dynamics of gas-phase collisions of hydrocarbons.

5.3.3 Additional Techniques

Finally, the experiments leveraged and proposed here rely on infrared spectroscopy and activation of NO-alkanes in the CH asymmetric stretching region. However, the optical parametric oscillator/amplifier (OPO/OPA LaserVision) is able to produce tunable IR radiation in the CH-stretch overtone ($\nu=2 \leftarrow \nu=0$) region. Therefore, it is plausible to obtain a resonant ion-depletion spectrum of NO-CH₄ and subsequent NO-alkane complexes in the overtone region. This capability would greatly help in characterizing the diverse set of interactions across all species and would be interesting to compare to the results acquired for the fundamental ($\nu=1 \leftarrow \nu=0$) CH asymmetric stretching region. Furthermore, equivalent infrared-activated dynamics studies would then follow by utilizing CH overtone infrared radiation. These studies would include infrared action spectra and subsequent velocity map imaging.

Additionally, the (1+1) resonant enhanced multiphoton ionization scheme affords us the ability to detect NO ($X^2\Pi$, $\nu'=0$, J' , F_n , Λ) products. Therefore, it would be plausible to employ this scheme to detect NO ($X^2\Pi$, $\nu'=1,2,3\dots$, J' , F_n , Λ) products. This would be important for techniques that rely on infrared activation of the NO-alkane complexes and subsequent detection of NO⁺ products. Therefore, this ability could be leveraged for infrared action spectra and velocity map imaging. By detecting NO in higher vibrational levels, such as $\nu'=1$, we would be able to reveal any mechanistic similarities are differences between

higher or lower energy NO products. These studies would be interesting to add to NO-CH₄ and would aid in characterizing the full dynamics outlook of this complex. This same scheme could, in practice, be applied to the longer chain NO-alkane complexes as well. Overall, this capability would aid in providing a rigorous understanding of how the energy flows into the co-products along the bimolecular collision pathway of these complexes. Therefore, this would aid in determining how these bimolecular collisions affect atmospheric and combustion chemistry.

5.4 References

- (1) Atkinson, R. Atmospheric Chemistry of VOCs and NO_x. *Atmos. Environ.* **2000**, *34* (12–14), 2063–2101. [https://doi.org/10.1016/S1352-2310\(99\)00460-4](https://doi.org/10.1016/S1352-2310(99)00460-4).
- (2) Tamé-Reyes, V. M.; Gardner, A. M.; Harris, J. P.; McDaniel, J.; Wright, T. G. Spectroscopy of the \tilde{A} State of NO–Alkane Complexes (Alkane = Methane, Ethane, Propane, and *n*-Butane). *J. Chem. Phys.* **2012**, *137* (21), 214307. <https://doi.org/10.1063/1.4768811>.
- (3) Musgrave, A.; Bergeron, D. E.; Wheatley, R. J.; Wright, T. G. Electronic Spectroscopy of the Deuterated Isotopomers of the NO-methane Molecular Complex. *J. Chem. Phys.* **2005**, *123* (20), 204305. <https://doi.org/10.1063/1.2125748>.
- (4) Akiike, M.; Tsuji, K.; Shibuya, K.; Obi, K. Van Der Waals Vibrations of NO–Methane Complexes in the $A_2\Sigma^+$ State. *Chem. Phys. Lett.* **1995**, *243* (1–2), 89–93. [https://doi.org/10.1016/0009-2614\(95\)00796-7](https://doi.org/10.1016/0009-2614(95)00796-7).
- (5) Crespo-Otero, R.; Suardiaz, R.; Montero, L. A.; García de la Vega, J. M. Potential Energy Surfaces and Jahn-Teller Effect on CH₄⋯NO Complexes. *J. Chem. Phys.* **2007**, *127* (10), 104305. <https://doi.org/10.1063/1.2752805>.
- (6) Holmes-Ross, H. L.; Gascooke, J. R.; Lawrance, W. D. Correlated Product Distributions in the Photodissociation of \tilde{A} State NO–CH₄ and NO–N₂ van Der Waals Complexes. *J. Phys. Chem. A* **2022**, *126* (43), 7981–7996. <https://doi.org/10.1021/acs.jpca.2c06312>.
- (7) Wang, X.-D.; Robertson, P. A.; Cascarini, F. J. J.; Quinn, M. S.; McManus, J. W.; Orr-Ewing, A. J. Observation of Rainbows in the Rotationally Inelastic Scattering of NO with CH₄. *J. Phys. Chem. A* **2019**, *123* (36), 7758–7767. <https://doi.org/10.1021/acs.jpca.9b06806>.
- (8) Daire, S. E.; Lozeille, J.; Gamblin, S. D.; Wright, T. G. The $\tilde{A} \leftarrow \tilde{X} (1 + 1)$ Resonance-Enhanced Multiphoton Ionization Spectrum of the NO·C₂H₆ and NO·(C₂H₆)₂ Complexes. *J. Phys. Chem. A* **2000**, *104* (40), 9180–9183. <https://doi.org/10.1021/jp001858d>.